Effects of ambient fluids on particle size segregation in saturated debris flows

Gordon G.D. Zhou[1,2], Kahlil F.E. Cui[1,2], Lu Jing[3,4], Tao Zhao[1,5], Dongri Song[1,2], Yu Huang[6]

[1] Key Laboratory of Mountain Hazards and Earth Surface Process, Chinese Academy of Sciences, Chengdu 61000, China

[2] Institute of Mountain Hazards and Environment, Chinese Academy of Sciences & Ministry of Water Conservancy, Chengdu 61000, China

[3] Department of Chemical and Biological Engineering, Northwestern University, Evanston, IL 60208, USA

[4] Department of Civil Engineering, The University of Hong Kong, Pokfulam Road, Hong Kong, China

[5] Department of Civil and Environmental Engineering, Brunel University London, London, UB8 3PH, United Kingdom

[6]Department of Geotechnical Engineering, College of Civil Engineering, Tongji University, Shanghai 200092, China

Corresponding author: Kahlil Fredrick Cui (kfcui@imde.ac.cn)

Key Points:

- Coupled fluid-particle simulations show that a viscous ambient fluid slows down size segregation.
- Ambient fluid affects segregation by reducing particle contact forces and through drag force-induced modification of shear rate profiles.
- Segregation velocities in different flow regimes follow a similar scaling if fluid effects are appropriately considered.

Abstract

Size segregation, which is a robust feature of sheared granular mixtures and geophysical mass flow deposits, is found to diminish in the presence of a viscous fluid. We study this inhibitive effect through coupled fluid-particle simulations of fully saturated granular flows. Granular-fluid mixture flows are modelled according to three distinct flow regimes – free-fall, fluid-inertial, and viscous – at different angles of inclination. Each flow regime corresponds to distinct flow dynamics and segregation behaviors. We find that segregation is indeed weaker and slower in the presence of an ambient fluid which is more so as the flow becomes more viscous. The ambient fluid affects segregation in two major ways. Firstly, buoyancy reduces the contact pressure gradients which are needed to drive large particles up, which at the same time reduces the particles' apparent weight. On the other hand, the streamwise drag force substantially changes the flow rheology, specifically the shear rate profile, thereby modifying the segregation behavior in the normal direction. Surprisingly, the fluid drag in the normal direction is negligible regardless of the fluid viscosity and does not affect segregation in a direct manner.

Key words: Size segregation, flow regimes, saturated granular flows, CFD-DEM

1 Introduction

Granular flows comprising particles of different sizes (Savage & Lun, 1988), shapes (Zhao et al., 2018; Mandal & Khakhar, 2019), and densities (Tripathi & Khakhar, 2013; Tunuguntla et al., 2014) have a tendency to segregate according to these species properties. Understanding and predicting segregation is relevant to processes where separation of different species may be either desired or avoided (Fan et al., 2014). Particle size segregation, with or without the presence of a viscous fluid, is of particular importance to geophysical flows, such as

debris flows and landslides (Johnson et al., 2012; de Haas et al., 2015), as it consequently leads to formation of run-out enhancing features such as flow-lubricating basal layers (Linares-Guerrero et al., 2007; Lai et al., 2017), channelizing levees (Johnson et al., 2012; Kokelaar et al., 2014; Baker et al., 2016), and coarse particle-rich heads (Gray & Ancey, 2009; Zhou & Ng, 2010; van der Vaart et al., 2018). Particle size segregation is also a significant process in riverbed armoring (Ferdowsi et al., 2017), grain sorting on the lee side of dunes (Kleinhans, 2004), and layer formation in faults (Siman-Tov & Brodsky, 2018; Itoh & Hatano, 2019).

Shear-induced size segregation in granular flows can be explained by the theory of kinetic sieving (Savage & Lun 1988; Vallance & Savage 2000), whereby small particles preferentially fall down into randomly generated voids beneath them while large particles are rolled up (Jing et al., 2017) to the free surface due to unbalanced contact forces (Gray & Thornton, 2005; Staron & Phillips, 2015). The downward percolation of small particles is stepwise, travelling down one layer at a time while sustaining minimal enduring contacts, as it makes its way through voids to the bed (van der Vaart et al., 2015; Jing et al. 2017). Large particles migrate upward “smoothly”, relying on the rearrangement and persistent contacts of the smaller particles around them (Jing et al., 2017). The fluctuating forces acting on large particles, when coupled with the local shear, can effectively push them up (Guillard et al., 2016; Jing et al., 2017; Staron, 2018). In addition to – or instead of – kinetic sieving is the percolation driven by kinetic stress gradients (i.e. velocity fluctuations, analogous to granular temperature) (Fan & Hill, 2011b; Hill & Tan, 2014) whereby large particles are segregated to regions of low kinetic stress (i.e. free-surface) (Dahl & Hrenya, 2004). Competing with the upward and downward percolation is the diffusive remixing which results from random collisions and shearing of

71 particles over each other (Gray & Chugunov, 2006). Diffusive remixing becomes more
72 significant in rapid flows where it results in a more diffuse and poorly-graded mixture.

73 In dry granular flows, the aforementioned micro-mechanisms result in inversely-graded
74 granular layers separated by a sharp concentration jump, the sharpness of which is determined by
75 the relative intensity of percolation and diffusive remixing. These processes are determined
76 under the assumption that the interstitial fluid is negligible. However, real-world granular flows
77 are water-laden (i.e. debris flows and mud flows) or are completely submerged (i.e. submarine
78 landslides and sediment flows), where solid-fluid interactions become significant and actively
79 influence the particle dynamics and subsequent re-arrangement (Coussot & Meunier, 1996;
80 Iverson, 1997). In such cases, segregation is not as evident or is completely absent depending on
81 various factors such as saturation (Major & Pierson, 1992; Zhou et al., 2019), grain-size
82 distribution (Zanuttigh & Ghilardi, 2010), and fluid properties (Vallance & Savage, 2000).
83 Although dry granular segregation has already been extensively studied, the role of fluids in this
84 process remains unclear. Through chute flow experiments of bi-disperse granular-fluid mixtures,
85 Vallance and Savage (2000) found that segregation in these cases is not as dramatic as dry flows
86 – the grading is more diffuse – indicating that the presence of fluids inhibits segregation. They
87 further concluded that segregation is weaker in water than it is in a more viscous yet less dense
88 fluid, which implies that the resulting inhibition depends on the relative densities of the particles
89 and the fluid phases rather than on the fluid viscosity. This was later confirmed by Thornton et
90 al. (2006) in which they derived, theoretically, that the percolation velocity decreases as the fluid
91 density approaches that of the particles and increases as the fluid becomes negligible. Likewise,
92 the direction of percolation velocities reverses when the fluid becomes denser than the particles
93 and no segregation occurs when the mixture is neutrally buoyant. Zanuttigh and Ghilardi (2010)

94 investigated the dependence of granular-fluid segregation on the average grain size and
95 concluded that the increased presence of larger particles slows down segregation as it allows
96 more fluid between voids which then reduces collision among particles.

97 The recurring theme presented by the handful of research on segregation in granular-fluid
98 mixtures is that the role of interstitial or ambient fluid is simply to inhibit segregation. Although
99 intuitive, a fundamental understanding of the mechanical origin of this inhibitive effect is still
100 missing. In particular, it is interesting to study whether the presence of a fluid affects segregation
101 directly through buoyancy and drag, or indirectly by modifying the shear profile and flow
102 rheology. Evaluation of these fluid effects on the segregation process will enable better
103 prediction of grading patterns in granular-fluid mixtures and understanding of the driving
104 mechanisms responsible for particle re-arrangement in natural granular flows.

105 The primary aims of this research is to isolate and evaluate different fluid effects in
106 granular segregation when the ambient fluid is non-negligible. To this end, simplified
107 simulations are conducted using a coupled fluid-particle approach, where three-dimensional fully
108 saturated, steady granular flows down an incline are simulated. The modelled system is
109 analogous to a section of a fluid-saturated debris flow or avalanche containing both coarse and
110 fine particles. Although size segregation is likewise dependent on the size ratio and the volume
111 concentration distribution (Hill & Tan, 2014; Tunuguntla et al., 2014; Jing et al., 2017), only the
112 effect of the angle of inclination is explored as we focus on how the emerging rheology affects
113 segregation. In the subsequent sections, we first lay out the theoretical background and the
114 research methodology. We then present results relating to (i) the mixture flow rheology, (ii)
115 different forces acting on the segregating particles, and (iii) partitioning of contact and kinetic
116 stresses. We then discuss how the presence of an ambient fluid affects size segregation and how

these findings might be used to explain the level of inverse grading observed in natural mass flow deposits.

2 Background

2.1 Mixture theory and stress partitioning

Isolation of fluid effects can be achieved by evaluating the relative significance of different forcing terms in the momentum equations of the mixture theory of segregation, which deals with the evolution of partial variables defined per unit volume, with each partial variable defined for a specific phase in the mixture (Gray, 2018). A unit volume (i.e. volume element over which partial variables are calculated) is denoted as V_M, and a size bi-disperse mixture composed of large (L) and small (S) particles, with a passive interstitial pore fluid (F) (e.g. air, water) is considered. For convenience, we use an index $i = L, S$ to collectively represent the large- and small-particle phases, while $i' = L, S, F$ for all three phases. The fraction of volume occupied by a mixture component i' is the volume fraction $\Phi_{i'} = V_{i'}/V_M$, and the total volume fraction sums to unity (Thornton et al., 2006):

$$\sum_{i'} \Phi_{i'} = 1 \quad \text{where} \quad i' = L, S, F \tag{1}$$

The solid concentration ϕ_i is the ratio between the volume fraction of a particle size species Φ_i and the total granular volume fraction $\mathbf{\Phi} = \Phi_L + \Phi_S$. The total solid concentration in a control volume also sums to unity, $\phi_L + \phi_S = 1$.

For a mixture of bi-disperse particles with a viscous interstitial fluid moving down an incline at a constant angle θ, in a coordinate system where the z-axis is pointing upward normal to the flow base, the x-axis along the direction of the flow, and the y-axis across the flow surface, the mass and momentum balances for each phase are given as:

$$\frac{\partial \Phi_{i'} \rho_{i'}}{\partial t} + \nabla \cdot (\Phi_{i'} \rho_{i'} \boldsymbol{U}_{i'}) = 0 \tag{2}$$

$$\frac{\partial}{\partial t}(\Phi_{i'} \rho_{i'} \boldsymbol{U}_{i'}) + \nabla \cdot (\Phi_{i'} \rho_{i'} \boldsymbol{U}_{i'} \otimes \boldsymbol{U}_{i'}) = -\nabla \cdot \boldsymbol{\sigma}_{i'} + \Phi_{i'} \rho_{i'} \boldsymbol{U}_{i'} + \beta \tag{3}$$

where $\boldsymbol{\sigma}_{i'} = \mathbf{1}\boldsymbol{P}_{i'} + \boldsymbol{S}_{i'}$ is the Cauchy stress where $\boldsymbol{P}_{i'}$ is the normal (called pressure for simplicity) and $\boldsymbol{S}_{i'}$ is the deviatoric component of the stress tensor. $\rho_{i'}$ is the phase material density and $\boldsymbol{U}_{i'} = (\boldsymbol{u}_{i'}, \boldsymbol{v}_{i'}, \boldsymbol{w}_{i'})$ is the partial velocity in three dimensions. The symbol $\otimes$ represents a dyadic product, and $\boldsymbol{g} = (g \sin\theta\,, 0, -g\cos\theta)$ is the gravity vector where g is the acceleration due to gravity. It follows that the total density and total stress are defined as $\rho = \Phi_L \rho_L + \Phi_S \rho_S + \Phi_F \rho_F$ and $\boldsymbol{\sigma} = \boldsymbol{\sigma}_L + \boldsymbol{\sigma}_S + \boldsymbol{\sigma}_F$ respectively.

The third term on the right-hand side of the momentum equation is the force exerted by one of the constituent phases on the others. In a three-phase mixture, this term can be further broken down into forces exerted by one solid component on the other $\beta^{L \leftrightarrow S}$, and forces exerted by the solid and fluid phases on each other $\beta^{G \leftrightarrow F}$. The solid interaction force is analogous to the percolation of fluids through porous solids and commonly adopts the form motivated by Darcy's Law (Gray & Thornton, 2005; Gray & Chugunov, 2006;):

$$\beta^{L \leftrightarrow S} = -\Phi_i \rho_i c_{PI} (\boldsymbol{U_i} - \boldsymbol{U}) - \boldsymbol{\Phi} \rho_G c_D \nabla \phi_i. \tag{4}$$

The first term in equation (4) expresses the relative velocity between the bulk and the individual phases where c_{PI} is the inter-phase drag coefficient. The final term represents diffusive remixing (Gray & Chugunov, 2006) where the coefficient c_D determines the strength of diffusion. The solid-fluid interaction term:

$$\beta^{G \leftrightarrow F} = \left(\boldsymbol{F}_i^b + \boldsymbol{F}_i^d\right)/V_M \tag{5}$$

154 is the sum of the buoyant force $\boldsymbol{F}_i^b$ and the drag force $\boldsymbol{F}_i^d$, acting on size species i per unit
155 volume. A more detailed evaluation of these forces is provided in Appendix A. We note that in
156 the three-phase mixture model of Thornton et al. (2006), the fluid phase is only assumed to exert
157 pressure on the surface of the particles. Here, we explicitly consider drag and buoyant forces
158 which result from the relative motion of the solid and fluid phases. Since the interaction terms
159 are internal forces, by Newton's Third Law, they should cancel as the mass and momentum
160 equations are summed over all phases, i.e. $\beta^{L-S} + \beta^{S-L} = 0$ and $\beta^{G-F} + \beta^{F-G} = 0$.

161 Following Fan and Hill (2011b), the total stress experienced by a particle $\boldsymbol{\sigma_i}$ is further
162 broken down into contact $\boldsymbol{\sigma}_i^c$ and kinetic $\boldsymbol{\sigma}_i^k$ components, representing the stresses which result
163 from particle contacts and velocity fluctuations, respectively. As segregation occurs long after
164 the bulk has reached a quasi-steady state, the temporal derivatives and inertial terms in the mass
165 and momentum balance equations can be set to zero. Assuming that the flow is shallow and that
166 segregation only occurs normal to the flow direction, the momentum equation can be reduced to:

$$0 = -\frac{\partial P_i^c}{\partial z} - \frac{\partial P_i^k}{\partial z} + \Phi_i \rho_i g \cos\theta - \Phi_i \rho_i c_{PI}(\boldsymbol{w_i} - \boldsymbol{w}) - \rho_G c_D \frac{\partial \phi_i}{\partial z} + \boldsymbol{F}_i^b / V_M + \boldsymbol{F}_i^d / V_M, \quad (6)$$

167 which can be simply denoted as:

$$0 = \Theta_i^{CS} + \Theta_i^{KS} + \Theta_i^W + \Theta_i^{PD} + \Theta_i^{FD} + \Theta_i^D. \quad (7)$$

168 Equation (7) implies that the forces acting on a particle phase i as it segregates are due to the
169 partial contact stress gradient Θ_i^{CS}, partial kinetic stress gradient Θ_i^{KS}, particle-particle drag Θ_i^{PD},
170 fluid drag Θ_i^{FD}, and diffusion Θ_i^D. Note that Θ_i^W is the buoyant weight that takes into account the
171 fluid buoyant effect.

In recent segregation models, it is assumed that as the small particles percolate down into the granular matrix they bear less of the overburden pressure while the larger particles bear most of it as they are squeezed up. Therefore, to define the share of the pressure a solid phase in a unit granular mixture bears, the pressure fraction ψ_i is introduced. The contact and kinetic pressure borne by each phase per unit volume can thus be represented as fractions of the total contact and kinetic pressures:

$$P_i^c = \psi_i^c P^c$$
$$P_i^k = \psi_i^k P^k \tag{8}$$

respectively. The pressure fractions ψ_i^c and ψ_i^k are assumed to satisfy the functional forms (Gray & Chugunov, 2006; Gray & Thornton, 2005):

$$\psi_{L,S}^c = \phi_{L,S} \pm B^c \phi_S \phi_L,$$
$$\psi_{L,S}^k = \phi_{L,S} \pm B^k \phi_S \phi_L, \tag{9}$$

respectively, such that $\psi_L^{c,k} + \psi_S^{c,k} = 1$, and $\psi_i^{c,k} = 0$ for $\phi_i = 0$. The coefficients B_c and B_k are the magnitudes of the 'overstress', which lead the partial pressures to be away from the hydrostatic pressure and indicates the strength of the segregation driving force. These values are expected to be positive and are dependent on the size ratio, shear rate, and possibly many other variables (Weinhart et al., 2013; Staron & Phillips, 2015). The opposing signs represent the premise that different sized phases experience different and oppositely directed stresses. Note that recent work has pointed out the asymmetric dependence of ψ_i on ϕ_i (Gajjar & Gray, 2014; van der Vaart et al., 2015; Jing et al., 2017). Here the simplest linear form is adopted, as it is sufficient for mixtures of a moderate solid species concentration (Fan et al., 2014; Schlick et al., 2015).

2.2 Segregation velocity scaling

The segregation velocity $w_{p,i}$ is the rate at which large and small particles separate from each other. It may be derived from the momentum equations, substituting equation (8) into equation (6) while disregarding the solid-fluid interaction terms, which yields a segregation velocity model that is dependent of the kinetic stress gradients (Hill & Tan, 2011) and gravity (Gray & Thornton, 2005); a key assumption in this derivation is that the solid interaction term depends linearly on the relative velocity (equation (6)). Alternatively, in the literature the scaling of $w_{p,i}$ is often directly inferred, grounded in the underlying physics of segregation. Savage and Lun (1989) found that the segregation velocity of a species increases proportionally with the local concentration of the opposite species, $w_{p,i} \simeq 1 - \phi_i$, i.e. large particles rise up faster when it is in a region with a high volume concentration of small particles, showing the importance of local packing on segregation. Golick and Daniels (2009) found that $w_{p,i}$ decreases with increasing confining pressures highlighting the dependence of segregation on dilatancy and void generation. When $w_{p,i}$ is scaled with the local shear rate, a good collapse is achieved reflecting the dependence of segregation on the local deformation rate (Fan et al., 2014; Schlick et al., 2015, Jing et al., 2017). In search of a functional form to express the pressure-shear rate dependence of $w_{p,i}$, Fry et al. (2018) proposed a scaling of the following form:

$$w_{p,i}/\sqrt{g\bar{d}} = \pm AI(1-\phi_i) \tag{10}$$

where $\bar{d}$ is the mean particle diameter, A is a dimensionless constant, and $I = \dot{\gamma}\bar{d}\sqrt{\rho_G/P_G}$ is the inertial number commonly used to define the rheology of dense granular flows (Midi, 2004). The

basic form of this scaling relation has been shown to work for both size and density-driven segregation for a wide range of situations (Umbanhowar et al., 2019).

The sensitivity of $w_{p,i}$ on the rheology of granular flows leads one to suppose that a similar functional form can be acquired for segregation in ambient fluids when the rheology of solid-fluid mixtures can be taken into account or if fluid effects can be appropriately considered. We note that an expression for $w_{p,i}$ has already been proposed by Thornton et al. (2006) which suggests that fluid affects segregation only through buoyant effects in such a way that segregation weakens when ρ_F approaches ρ_G. Though qualitatively consistent with physical experiments (Vallance & Savage, 2000), it does not consider any other forms of solid-fluid interactions and the resultant flow rheology.

2.3 Dimensionless characterization of flow regimes for granular-fluid mixtures

The role of viscous fluids varies significantly in different flow regimes. Therefore, it is crucial in this work to explore a wide range of flow regimes that are relevant to natural saturated debris flows. In dry granular flows viscous forces are negligible and the time it takes for a particle to travel a distance d, under a confining pressure P can be estimated from the time it takes for it to freely fall in air, $t_{FF} = d/\sqrt{P/\rho_G}$. The dynamics of granular flows in this regime is controlled by the inertial number $I = d\dot{\gamma}/\sqrt{P/\rho_G}$ which is the ratio of the microscopic inertial time to the shear rate $\dot{\gamma}$. When the viscosity of the ambient fluid η_F is high, the motion of particles is significantly hindered by the viscous forces. The particle momentarily accelerates before finally reaching its viscous limiting velocity after a characteristic time $t_V = \rho_G/P$. The flow dynamics in this regime is now controlled by the viscous number $I_v = \eta_F\dot{\gamma}/P$. According to Courrech du Pont et al. (2003), granular-fluid flows can be classified according to three regimes

– free-fall (grain-inertial), fluid-inertial, and viscous. Each regime is characterized by unique solid-fluid interactions and are controlled by three dimensionless numbers – the Stokes number $St = I^2/I_v = \rho_G d^2\dot{\gamma}/\eta_F$, the relative density $r_\rho = \sqrt{\rho_G/\rho_F}$, and the Reynolds number $Re = St/\ r_\rho\ -$ which express the relative importance of viscous and inertial forces on the flow rheology.

In the geophysical context, fluid-saturated granular flows can also be characterized according to the stresses and momentum transport processes which govern their motion. The Bagnold number $N_B = \left(\mathbf{\Phi}\rho_G\bar{d}^2\dot{\gamma}\right)/(1-\mathbf{\Phi})\eta_F$ defines the relative dominance between collisional and viscous forces where $\bar{d}$ is the mean particle diameter. The Savage number $N_S = \left(\rho_G\bar{d}^2\dot{\gamma}^2\right)/(\rho_G-\rho_F)gH\tan\zeta$ is the ratio between collisional and frictional forces where ζ is the inter-particle contact friction angle and H is the granular flow height. The friction number $N_F = (\mathbf{\Phi}(\rho_G-\rho_F)gH\tan\zeta)/(1-\mathbf{\Phi})\dot{\gamma}\eta_F$ is the ratio between frictional and viscous forces. These dimensionless numbers are typically used to classify the dominant energy dissipation mechanisms in natural (Iverson, 1997) and experimental (de Haas et al., 2015; Zhou et al., 2019) debris flows and subaqueous sedimentary density flows (Mulder & Alexander, 2001). Iverson (1997) proposed limits to the magnitudes of these dimensionless numbers to define the transition from one dominant mechanism to another based on dry, cohesionless, granular-flow experiments (Bagnold, 1954; Savage & Hutter, 1989). Collisional forces dominate over viscous forces when $N_B > 200$; collisional forces dominate over frictional forces when $N_S > 0.1$; and when $N_F > 2000$ frictional forces dominate over viscous forces.

3 Methods

3.1 Model configuration and simulation parameters

Fully saturated, binary granular flows are simulated using the coupled discrete element method (DEM) and computational fluid dynamics (CFD). This method enables calculation of solid-fluid interactions at relatively low computational costs allowing for efficient three-dimensional simulations. Calculations involved in the CFD-DEM method are detailed in Appendix A. For the DEM part, binary granular flows are simulated as a mixture of two types of inelastic, frictional spheres of distinct particle sizes (small and large) flowing down a rough incline. Small and large particles are set to have average diameters of $d_S = 0.005m$ and $d_L = 0.01m$ respectively. A slight poly-dispersity is introduced to each particle size to prevent geometrical ordering. This is implemented by randomly generating particles with diameters that are uniformly distributed around their mean value in such a way that $\frac{\left(d_{L,S}^{max} - d_{L,S}^{min}\right)}{d_{S,L}} = 0.1$ where d^{max} and d^{min} are the maximum and minimum diameters allowable for each particle size. The floor is roughened by 'gluing' a random array of small particles and no bounding walls are set at the top surface. This roughness condition ensures minimal slippage at the base. All DEM simulation domains are set to have a length, width, and height of $35d_S \times 10d_S \times 40d_S$. The size ratio and large particle concentration are held constant with values of 2 and 0.5, respectively, throughout all simulations since our focus is the fluid effects. Particles are initially normally graded – large particles locate at the base and small particles locate at the top.

Figure 1a shows the schematic diagram of the system being simulated and the corresponding coordinate system. Periodic boundary conditions are set along the flow direction representing an infinitely long chute and granular flows are initiated from rest by tilting the xy

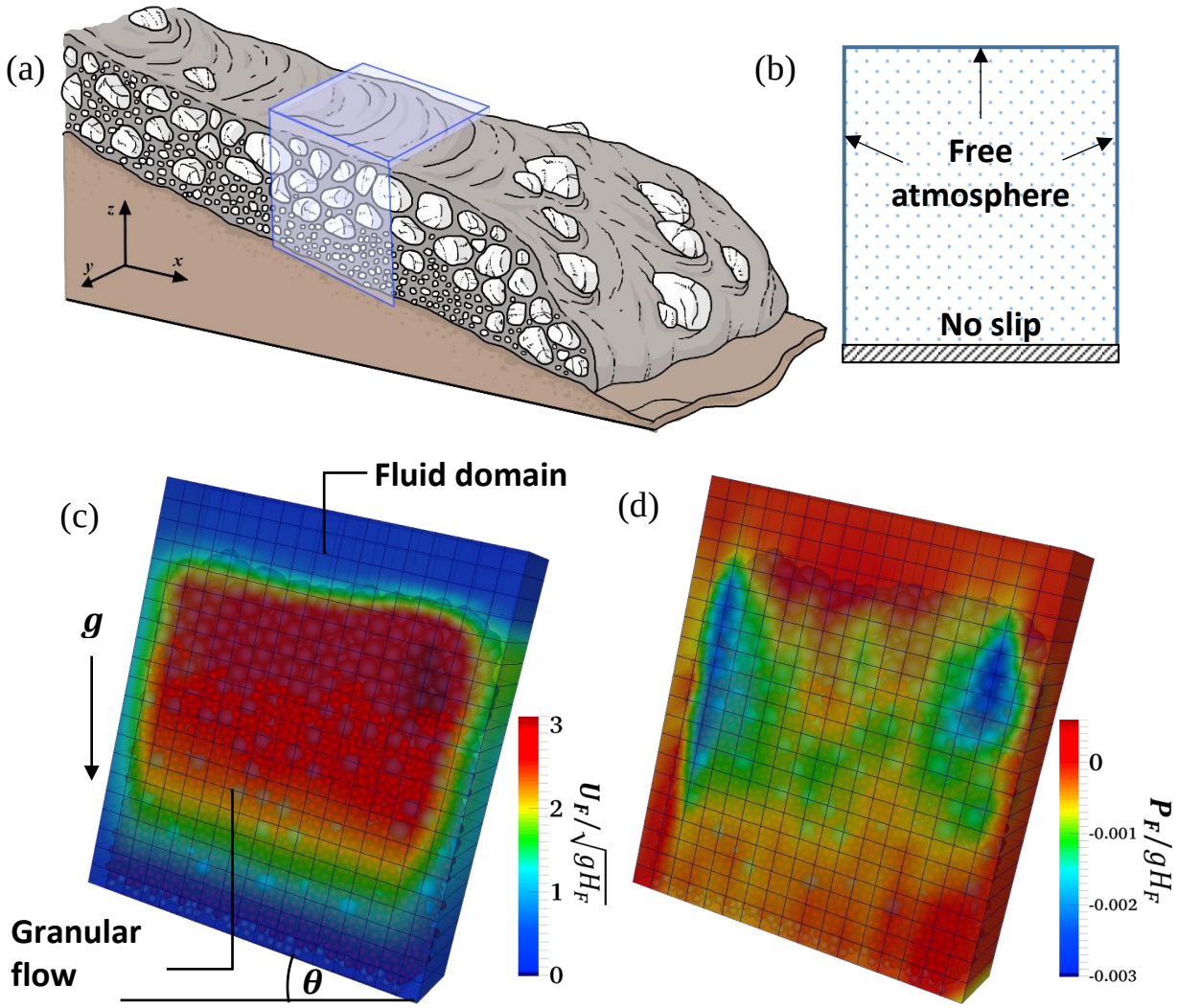

Figure 1. (a) A schematic diagram showing the simulated system – a fully saturated debris flow – and the coordinate system for a fixed section, indicated by the box. (b) Boundary conditions of the boxed domain in (a). Snapshots of (c) normalized fluid velocity $\boldsymbol{U_F}/\sqrt{gH_F}$ and (d) pressure $\boldsymbol{P_F}/gH_F$.

plane to a designated angle of inclination. The DEM solver in use can only set periodic boundaries in one direction at a time and hence rigid walls have to be placed lateral to the flow direction. Interactions between the lateral walls and the particles are set to be completely elastic and frictionless with the particle-wall contact stiffness equal to those between inter-particle collisions. We have verified that no velocity nor pressure gradients formed near the sidewalls.

Although wall-effects cannot be totally ruled out, they are found to have little effect on the segregation process and do not significantly change the main conclusions drawn from this work.

The fluid domain is an incompressible Newtonian fluid, uniformly discretized in such a way that at least five large particles would fit (Zhao et al., 2014). The fluid is ambient – it only responds to the drag exerted by the particles and does not flow on its own under gravity. As illustrated in Figure 1b, the state of ambience is obtained by adopting the free-atmosphere boundary condition at the right, left and top walls. Pressure is computed based on the local velocity of adjacent meshes where it is given a value p_0 if the flow is going out of the domain and $p_0 - 0.5\left|\boldsymbol{U_F^2}\right|$ for inflow; velocity dynamically changes from zero gradient when there is an outflow to flux dependent, computed as $-\nabla P_F$, when there is an inflow. This allows the fluid to freely flow in and out of the domain. A non-slip condition (zero pressure gradient, fixed zero velocity) is set at the bottom wall.

The complete simulation set-up is shown in Figure 1c where the solid domain is positioned completely within the fluid domain. The fluid is initially static and only flows as it is dragged by the particle motion. The normalized fluid velocity $\boldsymbol{U_F}/\sqrt{gH_F}$ fields **(**where H_F is the fluid height) match with the regions occupied by the moving grains, and therefore does not exert an external shear at the top surface of the granular flow. The rheology is completely controlled by the internal deformation of particles. Figure 1d, shows the distribution of the normalized dynamic component of the pore pressures $\boldsymbol{P_F}/gH_F$ within the granular flow. These pressures fluctuate rapidly with time wherein negative values correspond to shear expansion and positive values denote shear contraction. The negative pressure spikes at the edges of the granular flow

Table 1. *Model Input Parameters*

DEM Parameter	Value	Simulation parameter	Value
Young's modulus E (Pa)	5×10^{-7}	Simulation time t (s)	10^2 - 10^3
Poisson's ratio	0.35	DEM time step size Δt (s)	1×10^{-5}
Density ρ_s (kg/m^3)	2650	Coupling frequency*	10
Particle friction angle (°)	30		
Damping coefficient β	0.05		

*Coupling frequency is the number of the DEM iterations in one coupling interval.

domain (since the fluid domain is set slightly longer than the solid domain) result from the relative motion of the solid grains and the fluid (Zhao, 2017).

DEM particle and simulation parameters are kept constant throughout all simulations and are summarized in Table 1. It should be noted that, in order to minimize computation time, Young's modulus used in this study is lower than those of real glass beads. However, according to previous computational studies (Hill & Tan, 2014; Staron & Phillips, 2015; Jing et al., 2019) and some preliminary tests conducted, the choice of E, over a range of 10^7-10^9 Pa, does not significantly affect the flow properties at steady-state nor does it influence the development of size segregation. No cohesive forces resulting from the presence of ambient fluid is considered in the simulations.

3.2 Test set-up

The different flow regimes enumerated in II.C are simulated by varying the fluid density and viscosity. Mixtures flowing at different angles of inclination are simulated for each regime.

Table 2. *Test Setup*

Flow regimes	Inclination θ	$[\rho_F$ (kg/m^3), η_F (kg/m·s)]
Free-fall (FF)		$[1.29, 1.85 \times 10^{-5}]$
Fluid-inertial (FI)	[22, 24, 26, 28, 30, 32]°	$[1000, 1 \times 10^{-3}]$
Viscous (VI)		$[1000, 0.5]$

The free-fall (FF) regime corresponds to the dry case where the interstitial fluid is air and will serve as points of comparison as size segregation in dry granular chute flows have already been extensively studied (e.g. Tripathi & Khakhar, 2011; Tunuguntla et al., 2016; Jing et al., 2017). In the fluid-inertial (FI) regime, the ambient fluid is water at 20°C where the viscous forces are not high enough to dominate inertial effects for the latter to be completely ignored. A fluid 500 times more viscous than water is used in the viscous (VI) regime. This fluid is still Newtonian and has the same density as water. Such a fluid can be likened to the fine particle-rich slurries found in natural debris flows (Major & Pierson, 1992; Zhou & Sun, 2017) after it has already yielded. The fluid inertial and viscous regimes will be collectively referred to as the saturated regimes. The entire test setup is summarized in Table 2.

Segregation in different flow regimes will be analyzed according to the forcing terms enumerated in equation (7) and segregation velocities. As such, properties like the partial stress gradients, pressure fractions, flow velocities, shear rates, drag forces, etc. need to be calculated from DEM and CFD data. The method for calculating the said properties are detailed in Appendix B. It should be mentioned that the calculation of the contact pressure P^c is dependent on the manner at which forces are partitioned between differently sized particles. In this study, forces are partitioned according to the volume ratio of the contacting particles (Tunuguntla et al.,

2014) whereas several previous works partition the forces at the point of contact (i.e., according to the radius ratio of contacting particles) (Fan & Hill, 2011b; Staron & Phillips, 2015; Weinhart & Thornton, 2017). More information on the calculation and effects of the different contact force partitioning methods are presented in Appendix C. Likewise, the method for estimating the linear drag c_{PI} and diffusion coefficients c_D, which are necessary for the calculation of particle interaction forces, is discussed in detail in Appendix D.

4 Results

4.1 Dimensionless characterization of flow regimes

Simulated saturated granular flows are plotted in the (St, r_ρ) space as shown in Figure 2a. Each point falls within a specific flow regime bounded by limits proposed by Courrech du Pont et al. (2003) (solid lines) and Cassar et al. (2005) (dotted lines) which mark the transition from one regime to another. These points are calculated during rapid segregation time which will be defined in IV.B. To cast them into the light of actual geophysical flows, the Re values of the simulated flows are plotted against their N_B, N_S and N_F values as shown in Figures 2b, c, and d respectively. The dotted lines represent the boundaries proposed by Iverson (1997) and the gray areas are the range of values for the given dimensionless numbers obtained for natural debris flows (de Haas et al., 2015).

Flows in the FF regime are highly collisional and are primarily driven by grain-inertial forces as indicated by their very high Re and N_B values (Figure 2b). This is not surprising as the fluid in such cases are negligible such that they virtually do not affect particle motion. Flowing at relatively low angles of inclination, these flows are dense, more frictional than collisional as suggested by their N_S (Figure 2c). Increasing the flow velocity (by increasing the angle of

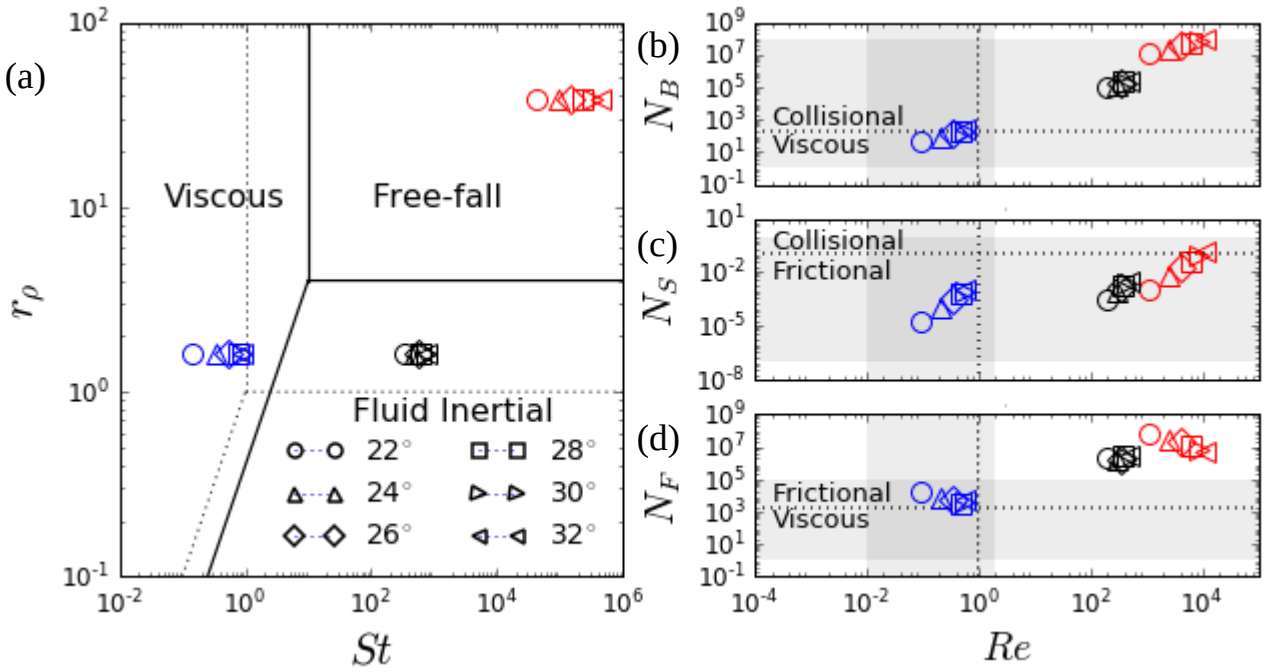

Figure 2. (a) Flow regimes of solid-fluid mixture flows projected in the (St, r_ρ) space. Solid lines represent the limits proposed by Courrech du Pont et al. (2003) which represent $\mathrm{St} = 10$, $r_\rho = 4$ and $\mathrm{Re} = 2.5$. Dotted lines are those assumed by Cassar et al. (2005) where $\mathrm{St} = r_\rho = \mathrm{Re} = 1$. (b-d) Simulated cases characterized by the dimensionless numbers for geophysical flows: (b) Bagnold number N_B, (c) Savage number N_S, and (d) Friction number N_F. Dashed lines represent the limits proposed by Iverson (1997) and shaded regions represent the ranges of the dimensionless numbers of natural debris flows summarized in de Haas et al. (2015). Symbols used in all plots represent the simulated cases at different angles of inclination ($\theta = [22,\ 24,\ 26,\ 28,\ 30,\ 32]°$).

inclination) makes the flows increasingly collision dominated. This is further supported by their N_F values where they become even more frictional than typical experimental and natural debris flows (Figure 2d).

The values of Re of the simulated FI flows are above the limits obtained for natural debris flows but are comparable to those of small-scale debris flow experiments (Iverson, 1997; de Haas et al., 2015). Their N_B values suggest that these flows are still highly collisional despite the presence of water (Figure 2b) but are more frictional than collisional based on the N_S values

(Figure 2c). This means that the viscous damping exerted by water is not enough to significantly inhibit grain-inertial effects but is enough to make them more frictional than subaerial flows (free-fall regime flows). The N_B and N_S values of the simulated fluid-inertial flows are comparable to those of typical natural debris flows (Figures 2b and c) approaching the limit of granular, hyperconcentrated density flows (Mulder & Alexander, 2001)

The dimensionless numbers of the simulated VI flows are close to natural debris flows but are lower than experimental debris flows. Their N_B values are consistently below the limit of viscous flows and their Re values suggest that grain-inertial effects are significantly low and these flows can be considered as ideally viscous (de Haas et al., 2015) (Figure 2b). Viscous damping becomes more significant in such flows making it increasingly frictional (Figure 2c). Measured friction numbers N_F however suggest that frictional forces still dominate over viscous forces (Figure 2d). This is due to the fact that shearing among particles is still due to the flow's downward motion by gravity and is only slightly viscous since the fluid itself is simply reactive to the granular flow.

4.2 Process of segregation

The degree of segregation, indicating how well the two particle-size species separate, is defined as the relative distance of separation between the large and small particles' centers of mass (Jing et al., 2017):

$$\alpha(t) = 0.5\left(1 - \frac{C_{L,t} - C_{S,t}}{C_{L,0} - C_{S,0}}\right) \tag{11}$$

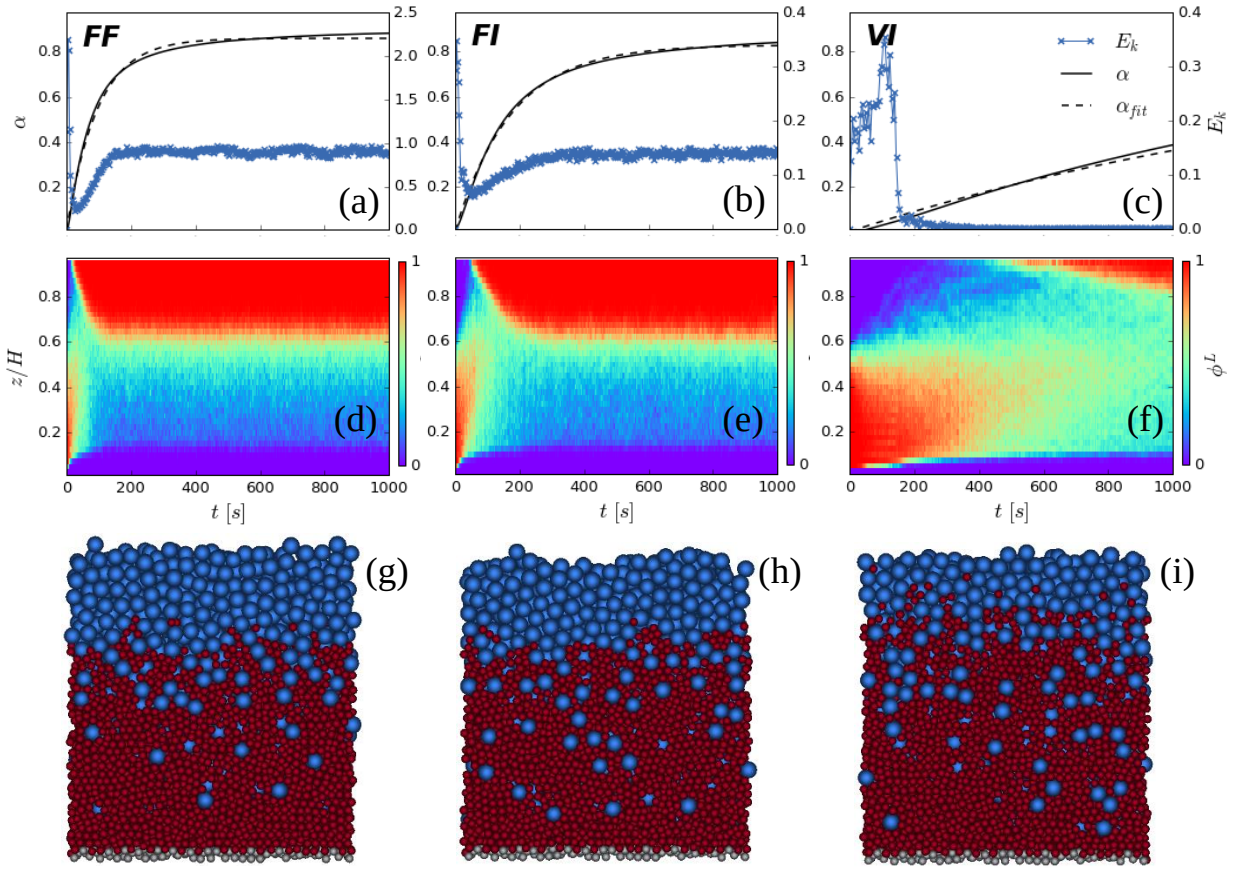

Figure 3. Arranged from top to bottom are (a-c) time evolution of the degree of segregation α and flow kinetic energy, (d-f) spatial-temporal distribution of the large particle concentration ϕ^L, and (g-i) final deposit profiles of the bi-disperse mixtures flowing at $\theta = 22°$ for different flow regimes. Dashed lines in (a-c) represent the fit obtained from equation (12).

where $C_{L,t}$ and $C_{S,t}$ are the bulk centers of mass of the large and small particles at time t, respectively, while $C_{L,0}$ and $C_{S,0}$ are the initial bulk centers of mass. A value of 1 represents perfect segregation, which means that the centers of mass of the two phases have completely reversed, while a value of 0 indicates that the mixture has not progressed from its initial state. Figures 3a-c show the evolution of α and granular flow kinetic energies E_k for the FF, FI, and VI regimes, respectively. At early times, α rapidly increases and slows down at a later point up until it reaches a steady state. The time evolution of α follows an exponential trend which can be fit to:

$$\alpha(t) = \alpha_f\left(1 - e^{-t/\tau_s}\right) \quad (12)$$

where α_f is the final degree at steady state, and τ_s is the dimensionless characteristic timescale associated with the segregation rate (Hill & Tan, 2014; Staron & Phillips, 2015) and reflects how fast segregation develops. Segregation is said to develop faster when the values of τ_s is small, and slower otherwise. To illustrate how well α represents the process of segregation, the corresponding spatial-temporal profiles of the large particle concentration ϕ_L are plotted in Figures 3d-f for the FF, FI, and VI regimes, respectively. Snapshots of the three segregated mixtures at the end of the simulation are shown in Figures 3g-i. Due to computational limitations all simulations have only been run up to $t = 1000s$, by which time segregation in VI is still incomplete. Nevertheless, in this study we are more interested in the segregation process rather than the steady state and we focus on the time when segregation is still underway.

Figure 4a shows that the α curves for a similar angle (22°) belonging to different flow regimes can be cast into a single time frame when they are plotted against the dimensionless time t/τ_s. The shaded area represents a period of time $t = 0{\sim}0.5\tau_s$ in which segregation in the three regimes can be considered to develop at the same pace. The value of α achieved at $0.5\tau_s$ (denoted as $\alpha_{0.5\tau_s}$) for all θ are plotted in Figure 4b, showing that the degree of segregation generally decreases with the inclination but are comparable across different flow regimes. For the FF and FI cases, maximum segregation is achieved at the lowest angle $\theta = 22°$, while for the VI cases, optimal segregation occurs at a medium angle $\theta = 24°$, after which α declines steadily.

Figure 4c shows the segregation time scale τ_s (inversely, the characteristic segregation rate) for the three flow regimes. Interesting trends are observed. In dry cases (FF regime), τ_s

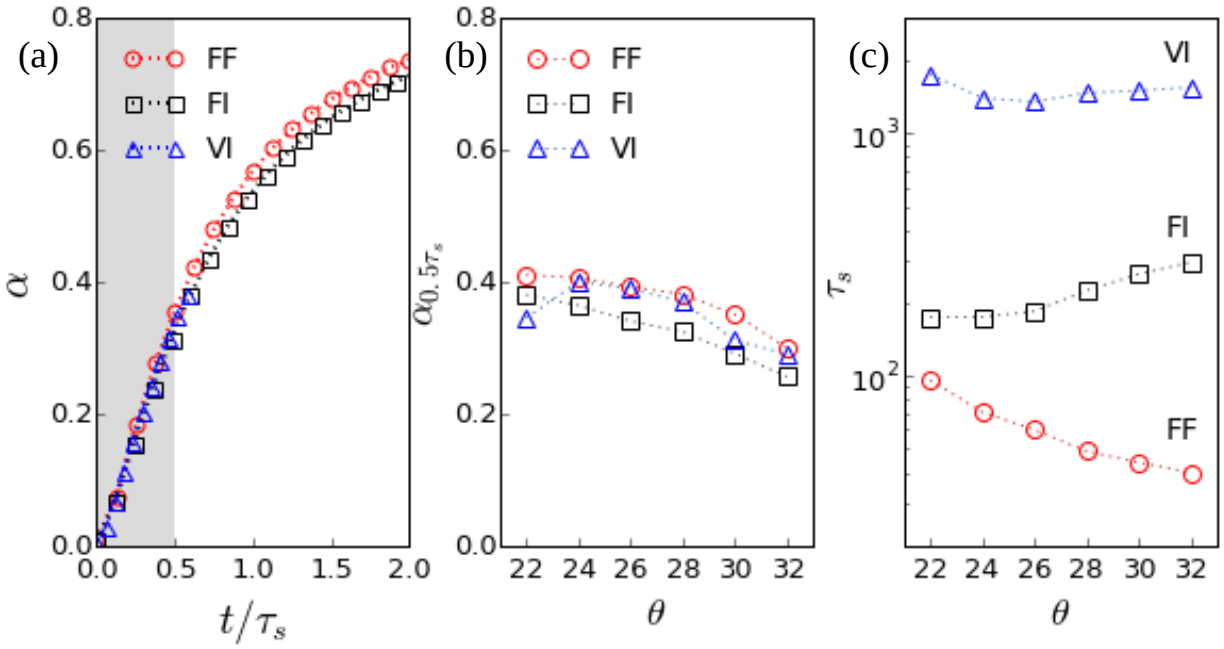

Figure 4. (a) Evolution of the degree of segregation α for $\theta = 22°$ for all flow regimes in dimensionless time t/τ_s. The gray region indicates the span of time in which the segregation in the three regimes develop simultaneously. (b) $\alpha_{0.5\tau_s}$ vs. θ and (c) τ_s vs. θ for all flow regimes.

decreases as θ is increased; qualitatively, this can be understood as faster flows result in faster void generation and kinetic sieving (Drahun & Bridgwater, 1983). In saturated cases, τ_s is generally increased, consistent with previous chute flow experiments of Vallance and Savage (2000). However, the trend of τ_s with θ is reversed in the saturated regimes where segregation instead develops over longer periods of time when θ is increased. To investigate this, we look into the flow rheology and driving forces in the momentum equations which are measured during the segregation process.

4.3 Mixture flow rheology

Figure 5 shows the profiles of the bulk flow velocity u, shear rate $\dot{\gamma}$, contact pressure P^c, and kinetic pressure P^k of all cases. These profiles are averaged over $t = 0.1{\sim}0.5\tau_s$ where segregation is considered to develop rapidly and the initiation effects are minimal. The pressures

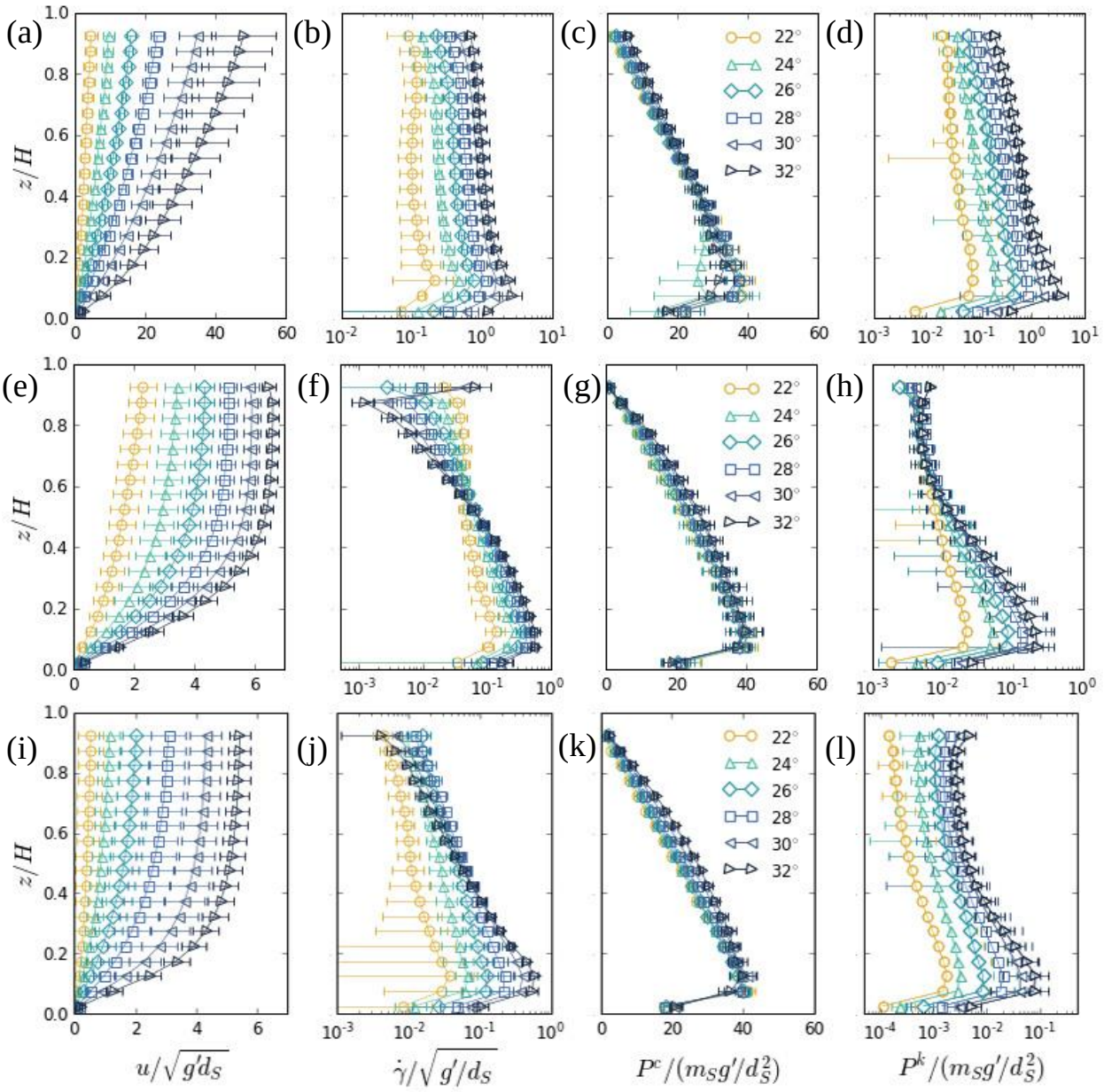

Figure 5. Dimensionless, time-averaged u, $\dot{\gamma}$, P^c, and P^k profiles of granular-fluid flows in the (top) FF, (middle) FI, and (bottom) VI flow regimes for different angles of inclination. Averaging is done over the time when segregation is rapid.

are normalized by $m_S g'/d_S^2$ where m_S and d_S are the small particle mass and diameter, respectively, and $g' = (\rho_G - \rho_F)g/\rho_G$ is the reduced gravity due to buoyancy. u and $\dot{\gamma}$ are normalized by $\sqrt{g'd_S}$ and $\sqrt{g'/d_S}$, respectively. The z coordinate is normalized by the granular flow height H. The error bars represent the standard deviations of the measured quantities.

In the FF regime, u increases with θ and shows no slippage near the base (Figure 5a), $\dot{\gamma}$ varies linearly along the height except near the base and also increases with θ (Figure 5b), P^c increases towards the base and only changes slightly with θ (Figure. 5c), and P^k, which measures random particle fluctuations, scales similarly with the shear rate (Figure 5d). The shapes of all rheological profiles do not significantly vary for different values of θ but consistently increase in magnitude.

In the FI regime, plug zones are observed near the free surface of the u profiles (Figure 5e). This flow feature is similar to what is observed in subaqueous laboratory sediment flows (Ilstad et al., 2004) and experimental debris flows (Mainali & Rajaratnam, 1994). We attribute the origin of plug zones to the fluid drag force in the flow direction, which changes the rheological behavior of the flows (more data are provided in Appendix C). The plug zone corresponds to an area of very low $\dot{\gamma}$ in which the velocity differences between flowing layers are small (Figure 5f). P^k in this regime is lower by about an order of magnitude compared to that in FF, implying that the random fluctuating motion of both particle species are greatly suppressed (Figure 5h). Below the plug zone, u rapidly decreases as it approaches the base, corresponding to the rapid increase of $\dot{\gamma}$ and $P^k.P^c$, being normalized by g', has the same magnitude as that of the FF regime, showing that the ambient fluid reduces the magnitude of the normal contact forces between particles (Figure 5g), i.e., a hydrostatic buoyant effect. The dynamic component of buoyancy along the normal direction is found to be negligible.

In the VI regime, u values are only slightly lower than those in FI and similar plug zones are observed (Figure 5i). $\dot{\gamma}$ is observed to increase with θ up to 28° and start to decrease at higher angles between 30° and 32° (Figure 5j). These rheological behaviors are linked to the fluid-

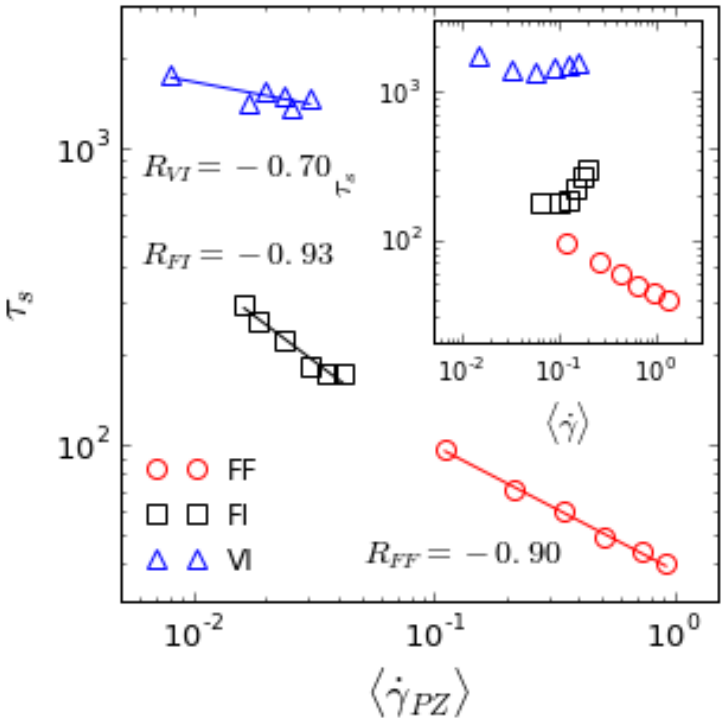

Figure 6. The relationship between the segregation timescale τ_s and the averaged shear rate measured in the plug zone $\langle\dot{\gamma}_{PZ}\rangle$ and (inset) along the entire flow depth $\langle\dot{\gamma}\rangle$. The strength of correlation between these two values is measured by the Pearson coefficient R. Fitting lines are obtained using the equation $y = ax^b$.

particle interactions in the VI regimes and are explained in more detail in Appendix C. P^k is lower by an order of magnitude relative to FI (Figure 5l). P^c is still of the same magnitude as with the previous two regimes and vary only slightly with θ, since the buoyant effect is a function of the relative density of the solid and fluid phases and is independent of the fluid viscosity (Figure 5k).

To link segregation with the flow rheology, $\dot{\gamma}$ is plotted against the segregation timescale τ_s as shown in Figure 6. The $\dot{\gamma}$ is singled out among all rheological profiles since it is the one showing the greatest sensitivity to the flow conditions and, as reported in several previous studies (May et al., 2010; Staron & Phillips, 2014), is strongly related to the segregation timescale. The inset of Figure 6 shows that the depth-averaged shear rate $\langle\dot{\gamma}\rangle$ generally increases

with θ in all flow regimes and thus, as with Figure 4c, τ_s decreases in FF but increases in FI and VI as $\langle\dot{\gamma}\rangle$ increases. Plotting τ_s against $\langle\dot{\gamma}_{PZ}\rangle$, which is the average shear rate in the plug zone (which occupies approximately the upper half of the $\dot{\gamma}$ profile excluding the topmost points), yields consistently decreasing trends across all flow regimes with strong negative correlations (shown as Pearson R correlation coefficients in Figure 6). The changes of $\langle\dot{\gamma}_{PZ}\rangle$ with θ in VI is consistent with the non-monotonic trend of τ_s – the decrease of $\langle\dot{\gamma}_{PZ}\rangle$ starting from $\theta = 28°$ matches the increase of τ_s at the same angle. This implies that in addition to the reduction of total $\dot{\gamma}$ across different flow regimes, segregation is also sensitive to the formation of fluid-induced rheological features such as plug zones.

4.4 Momentum balance source terms

Figure 7 shows the depth-averaged 'forces' acting on the rising large particles in the normal direction for mixtures flowing at 22° for $t = 0{\sim}0.5\tau_s$ (the shaded region in Figure 4a). These forces correspond to the source terms on the right-hand side of equation (7). In this way, the forces acting on the large particles can be compared directly during the time in which segregation in the three flow regimes occur at the same pace, facilitating the isolation of different fluid effects and comparison of their magnitudes with those induced by particle interactions. All force terms are normalized by the buoyant weight prior to depth averaging to take into account the buoyant effect.

At the onset of segregation the partial contact stress gradient Θ^{CS} is larger than the bulk buoyant weight Θ^{W} (see, e.g., Figure 7a), and therefore drives the large particles upward. By contrast, the kinetic stress gradient Θ^{KS} remains small in all stages. As segregation proceeds, Θ^{CS} decreases as more particles rise up to the free surface. It is interesting to note that the difference

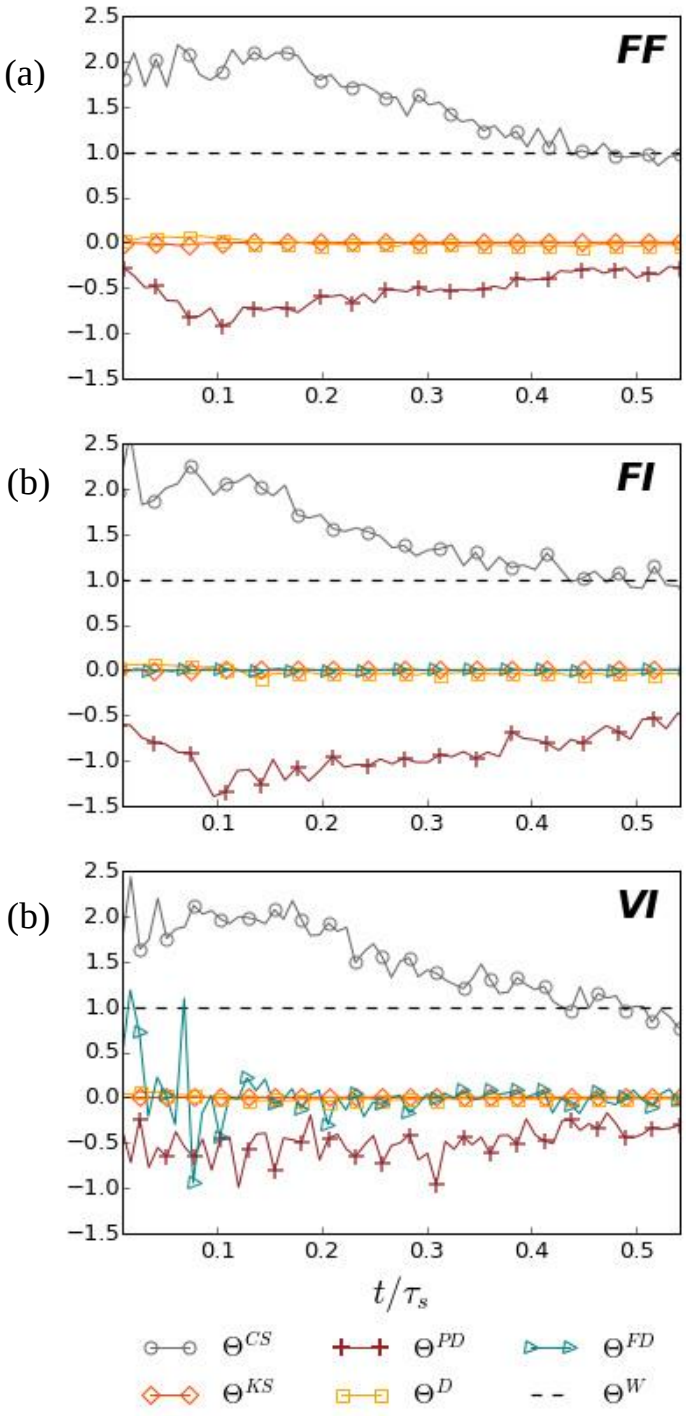

Figure 7. Time evolution of the force terms experienced by large particles according to equation (7).

between Θ^{CS} and Θ^{W} are comparable in all three flow regimes (Figures 7a-c), indicating that buoyancy reduces the weight and the partial pressure gradient in a similar way. Therefore, it can

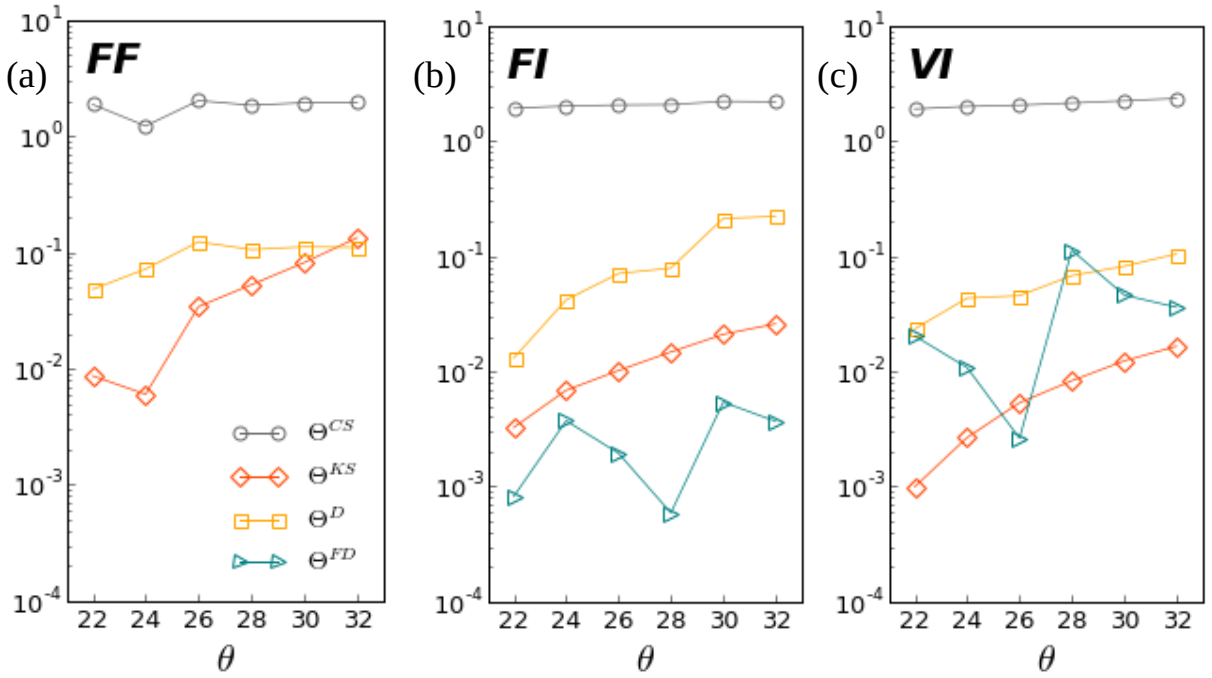

Figure 8. Magnitude of the mean forces acting on the large particles in the (a) FF, (b) FI, and (c) VI regimes as functions of θ.

be concluded that the buoyant effect mainly acts as a scale factor for gravity, which warrants the use of the reduced gravity g'.

The difference between Θ^{CS} and Θ^{W} is mainly balanced by the particle-particle drag, Θ^{PD} (and only slightly by the diffusive force Θ^{D}), while the fluid-particle drag Θ^{FD} is practically negligible in both two saturated regimes (with larger fluctuations in the VI regime). The latter is a surprising result as the fluid viscosity in the VI regime is high. Close evaluation of the fluid drag force shows that, since segregation proceeds slowly in the VI case, the drag forces are negligible owing to the very small relative velocities between the large particles and the fluid along the normal direction.

To understand the dependence of the segregation time on the slope angle (Figure 4c), we average each force term over $t = 0{\sim}0.2\tau_s$ for all simulated cases and plot their absolute values against θ in Figure 8. The choice of this time span is quite arbitrary and is only considered since

it corresponds to the time in which Θ^{CS} is the highest in all simulated cases. Figure 8 shows that Θ^{CS} is similar in magnitude and varies only slightly with θ regardless of the flow regime, while Θ^{KS}, although small in magnitude, increases significantly with θ. The level of diffusion (Θ^{D}) steadily increases with θ even with the presence of a viscous fluid and is roughly of the same order of magnitude relative to Θ^{KS} in each flow regime. In the saturated regimes, Θ^{FD} values are consistently low and show no clear dependence on θ.

Results in Figures 7 and 8 suggest that segregation occurs when the partial normal stress gradient in the mixture overcomes the pull of gravity, as is the premise of gravity-driven segregation theory (Gray & Thornton, 2005). This is a robust result across the three distinct flow regimes, as long as the buoyant effect is taken into account. However, within each flow regime, the dependence of the segregation time scale on the inclination angle (hence local shear rates) cannot be explained by this argument because Θ^{CS} only varies mildly with θ, which does not match the trend of τ_s with θ. Furthermore, Θ^{CS} decays toward and even below Θ^{W} far before the process of segregation completes (Figure 7). This indicates that the depth-averaged stress gradient, although capturing the fluid buoyant effect, may smear out fine details regarding distributions of the local concentration and the local shear rate, a point we address further below.

4.5 The overstress coefficient B

As the dependence of segregation driving force on θ is not well-captured by depth-averaging, a more localized approach is adopted here to take into account the local concentration. According to the gravity-driven segregation theory, segregation occurs only when the fraction of the pressure ψ_i experienced by a particle species is greater than what the local concentration ϕ_i can support. This relationship is expressed using equation (9) where the partition coefficient B

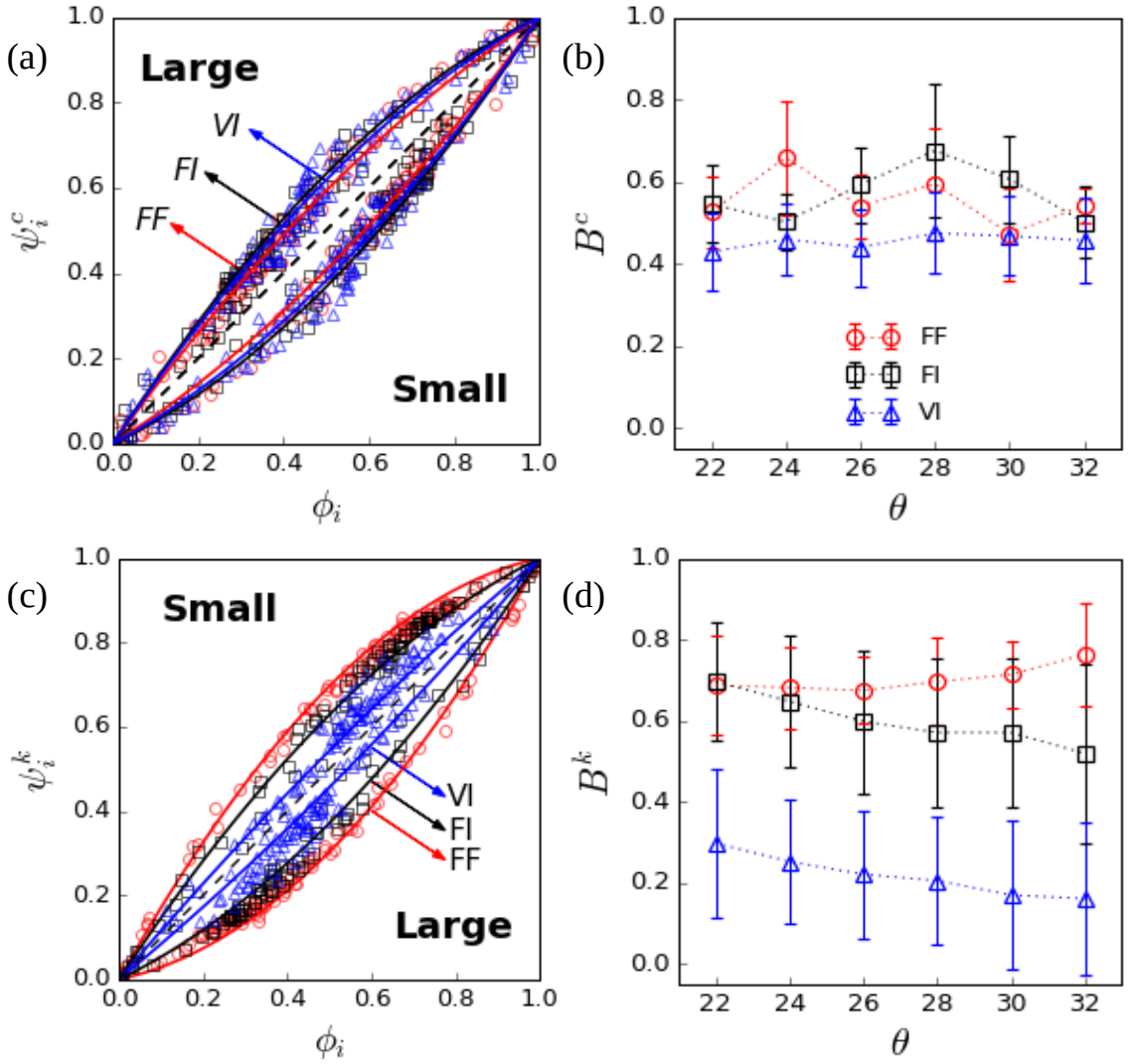

Figure 9. (a) Contact stress fraction ψ_i^c as a function of the volume concentration ϕ_i during rapid segregation of mixtures flowing at 22° in different flow regimes. (b) B^c values as a function of θ. (c) Kinetic stress fraction ψ_i^k vs ϕ_i and (d) B^k as a function of θ.

indicates by how much ψ_i is greater than ϕ_i and hence measures how strong the segregation driving force is. This analysis is applied for both contact and kinetic pressures.

The contact stress fraction ψ_i^c for different flow regimes ($\theta = 22°$) are plotted as functions of ϕ_i in Figure 9a. The contact stress fraction of large particles are larger than their concentrations, which means that the large particles bear more of the contact pressure relative to the small particles. The $\psi_i^c - \phi_i$ curves of the FF, FI, and VI regimes are closely overlapping,

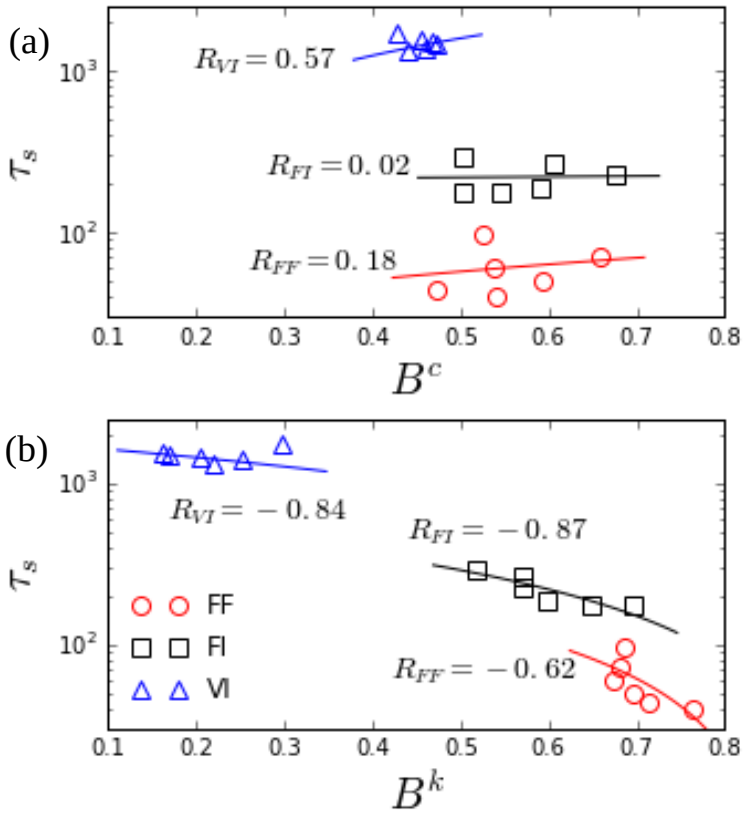

Figure 10. The relationship between τ_s and (a) contact B^c and (b) kinetic B^k overstress coefficients, with the strength of correlation measured by the Pearson coefficient R. Fitting lines are obtained using the equation $y = ax^b$.

where positive B^c values of $0.58, 0.56$ and 0.47 for the large particles are obtained, respectively, suggesting that the biased contact stress distribution act in the same direction of their upward motion. (Note that these values are significantly higher than those reported in Hill and Tan (2014), due to the different partitioning criteria applied; see Appendix B2.) Figure 9b shows that B^c is essentially independent of θ, and is noticeably lower in the VI regime than in the FF and FI regimes. Figure10a shows that B^c is only weakly correlated with τ_s, which is similar to the correlation regarding Θ^{cs} in Figure 8.

The relationship between the kinetic stress fraction ψ_i^k and ϕ_i is shown in Figure 9c. Fitting equation (9) for the large particles yields negative values of $B^k = -0.72, -0.70$ and -0.35 for the FF, FI, and VI regimes respectively. Positive B^k values for the small particles

525 mean that they are the ones bearing more of the kinetic pressure. Figure 9d shows that B^k
526 increases with θ in the FF regime but decreases in the fluid-saturated regimes. B^k also decreases
527 as the flow becomes more viscous – it is highest in the dry FF regime and lowest in the VI
528 regime. This is consistent with the global decrease in P^k by orders of magnitude, observed in
529 Figure 5, as the flows become more viscous. Figure 10b shows that B^k is significantly negatively
530 correlated with τ_s, which is likely due to the similar dependence of P^k and τ_s on $\dot{\gamma}$.

531 Comparing Figures 7 and 8 shows that both Θ^{KS} and B^k are sensitive to θ but exhibit
532 dissimilar trends despite both being measurements of the partial kinetic stress. The difference
533 may be attributed to the manner in which they are calculated. Since Θ^{KS} is a depth-averaged
534 quantity it does not capture the drastic changes in the kinetic pressure profiles which, for
535 instance, result from formation of plug zones or accumulation of large particles at the flow
536 surface. These localized effects are better captured by B^k, which is obtained with the functional
537 form (equation (10)) encoding the effect of the local concentration ϕ_i.

538 4.6 Scaling relationship for the segregation velocity

539 The segregation velocity $w_{p,i}$ measures how fast segregating particles move away from
540 each other. Recently, scaling relationships for $w_{p,i}$ have been used to highlight the mechanisms
541 relevant to segregation in different geometries and under different flow conditions, where data
542 points ideally collapse onto a single curve when normalized by appropriate functional forms.
543 Likewise, determining the appropriate scaling relationship for $w_{p,i}$ in different flow regimes
544 encountered here will ideally shed light on the primary mechanisms of segregation in the
545 presence of ambient fluids.

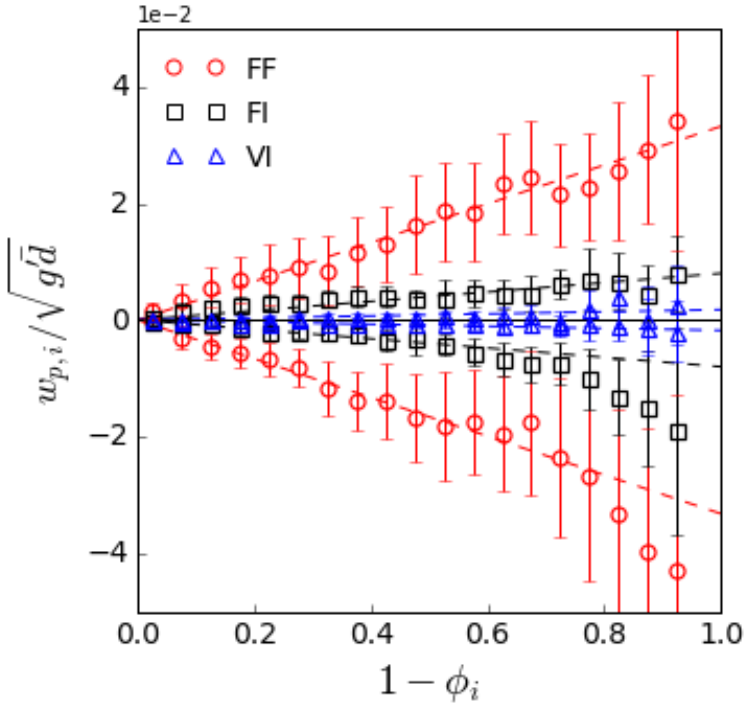

Figure 11. Dimensionless segregation velocities of large and small particles for each flow regime (averaged over all θ) as a function of $1-\phi^i$.

The mean dimensionless segregation velocities for each regime is plotted as a function of $1-\phi_i$ in Figure 11. Note that the data points (and error bars) represent the means (and standard deviations), obtained from each regime, averaging over all cases with varying θ. Although in each regime the slope of the curves depends slightly on θ (consistent with the trend in Figure 4c), the variation is negligible when comparing them across flow regimes (raw data prior to averaging are presented in Appendix D). Figure 11 shows that $w_{p,S}$ and $w_{p,L}$ increase significantly in magnitude across the three flow regimes, and in each regime the segregation velocity depends linearly on $1-\phi_i$. The slopes of the linear fit are equal in magnitude for both large and small particles. Recently, Jones et al. (2018) have shown that the dependence of $w_{p,i}$ on $1-\phi_i$ can be better described using a quadratic equation which further takes into account the asymmetric dependence of $w_{p,i}$ on the local concentration. The same asymmetry is observed in

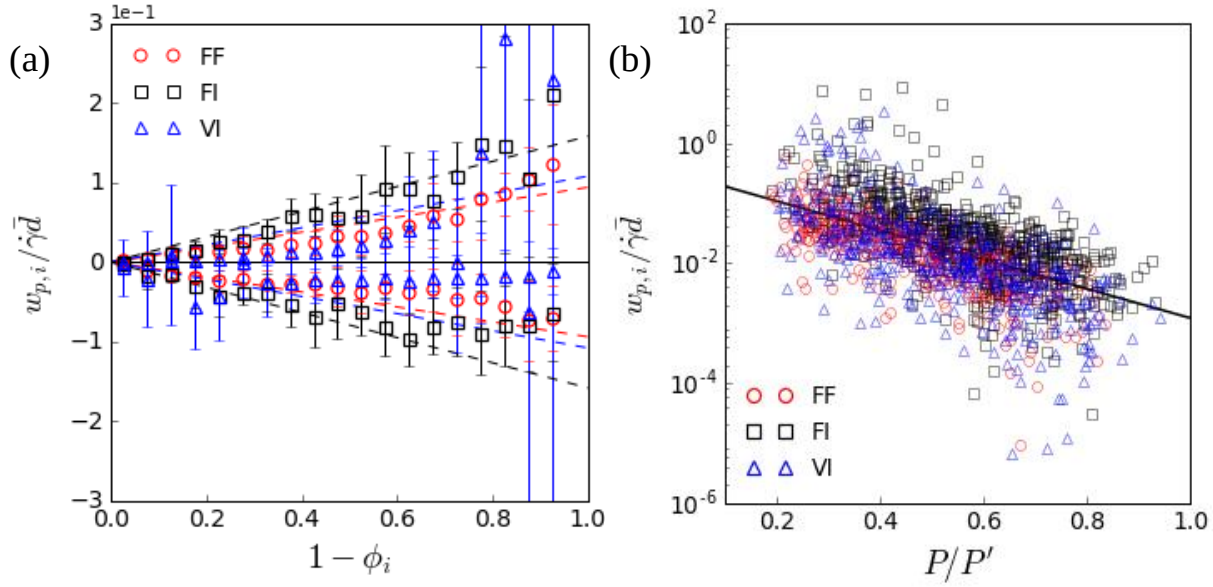

Figure 12. (a) Segregation velocities normalized by local shear rates vs. $1-\phi_i$. Dashed lines are obtained using a linear fit. (b) The same normalized velocities versus the local total normal stress normalized by the reduced pressure $P' = \boldsymbol{\Phi}(\rho_G - \rho_F)gH\cos\theta$. The fitting line is an exponential function $y = 0.3e^{-5.8x}$.

Figure 11 where $w_{p,S}$ is indeed greater than $w_{p,L}$, especially at higher $1-\phi_i$, indicating that small particles, in the presence of more large particles, sink faster compared to the rise of large particles surrounded by the opposite size species. In this study, a simple linear dependence is nevertheless adopted as it is sufficient to illustrate the fluid effects on $w_{p,i}$ across the different flow regimes.

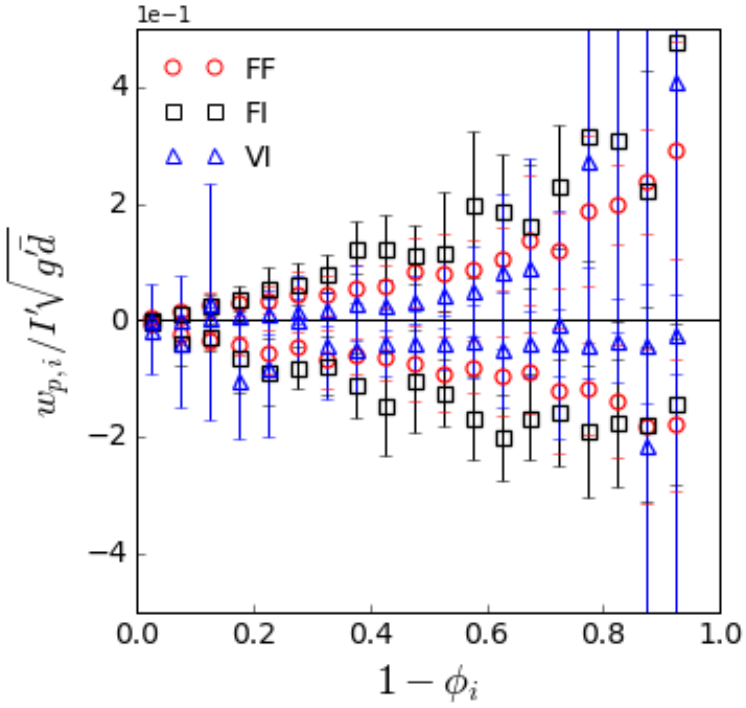

Figure 13. The segregation velocity of large particles for different flow regimes (averaged over all θ) normalized by the reduced inertial number I'.

The slopes in the two saturated regimes (FI and VI) are generally lower than that in FF. Normalizing $w_{p,i}$ by $\dot{\gamma}\bar{d}$, as shown in Figure 12a, drastically changes the slopes of the curves, largely collapsing the data from different regimes. To see whether the collapse can be further improved, we check for pressure dependence by plotting the logarithm of the normalized segregation velocity $w_{p,i}/\dot{\gamma}\bar{d}$ against the dimensionless total pressure $P/\mathbf{\Phi}(\rho_G - \rho_F)gH\cos\theta$ as shown in Figure 12b. The local segregation velocities from different flow regimes show a slight negative correlation with the normalized pressure. The significant scattering is perhaps due to the exclusion of local concentrations.

The results presented thus far show that the most obvious effects of fluid on segregation are manifested through the reduction of the shear rates and the pressure. Fluid viscosity is not found to have any direct effect on the upward and downward percolation of particles and only

works to provide more viscous dissipation in the flow direction, thus further decreasing the shear rate and the kinetic pressure. We summarize these effects by proposing a slight modification to the scaling relationship by Fry et al. (2018):

$$w_{p,i}/\sqrt{g'\bar{d}} = \pm AI'(1-\phi_i) \tag{13}$$

where $I' = \dot{\gamma}\bar{d}\sqrt{\rho_G/P'}$ is the reduced inertial number and $P' = \mathbf{\Phi}(\rho_G - \rho_F)(H-z)g\cos\theta$ is the reduced pressure which takes into account the effect of buoyancy. A is a dimensionless proportionality constant which may be dependent on the size ratio and relative concentration of size species. The signs represent the direction of the percolation.

In Figure 13, the mean dimensionless segregation velocities for both large and small particles are scaled using the reduced inertial number I' and are plotted against $1-\phi_i$. There is very little change from the trends shown in Figures 12a, which means that the additional consideration of the pressure has a limited effect on the scaling of the segregation velocity. We have attempted to use other functional forms which quantify the rheology of granular-fluid mixtures, such as the viscous number I_v (Cassar et al., 2013) and viscous-inertial numbers proposed by Trulsson et al. (2012) and Amarsid et al. (2017), instead of I', but find very little improvement with the scaling.

5 Discussion

5.1 Size segregation in solid-fluid mixtures

Our simulations show that segregation in solid-fluid mixtures are slower and weaker (related to the degree of segregation α) than when the interstitial fluid is negligible. These results are qualitatively consistent with experiments conducted using chute flows (Vallance & Savage,

2000; Zanuttigh & Ghilardi, 2010). In simulated saturated flows, however, it is observed that the time it takes to segregate increases as the inclination is increased, contrary to what is observed in dry flows. The ambient fluid exerts a drag force in the flow direction counter to the motion of the granular flow, which leads to the formation of a plug zone near the flow surface, corresponding to a region of very low shear rates, thereby slowing down segregation. The only solid-fluid interaction that is significant along the normal direction is the buoyant force; normal drag forces are negligible regardless of the viscosity of the ambient fluid.

Evaluating normal volume-averaged forces acting on the rising large particles shows that the main force opposing gravity is the partial contact stress gradient, implying that such gradients drive the large particles up. The buoyancy provided by the ambient fluid reduces inter-particle contacts but at the same time helps support the weight of the rising particles, and effectively works as a scaling factor for the bulk weight. The work of Thornton et al. (2006) shows that this buoyant effect results from the relative densities of the solid and fluid phases such that the closer the densities of the two phases the weaker the segregation. The chute flow experiments of Vallance and Savage (2000) also show that the effect of the relative densities are more significant than that of viscosity. Although this work does not explore the effect of fluid properties in great detail, it can be seen that having similar fluid densities between the FI and VI regimes results in approximately equal partial pressure gradients despite very different ambient fluid viscosities.

However, although contact stress partitioning captures the first-order effect of buoyancy across flow regimes, it fails to describe the detailed dependence of the segregation time scale on the inclination angle (i.e., local shear rates). Neither the depth-averaged contact stress gradient Θ^{CS} nor the contact stress partitioning coefficient B^c show clear correlation with τ_s. These results

imply that although particle contacts indeed drive the large particles upward, as supported also by recent force measurement research (Guillard et al., 2016; van der Vaart et al., 2018), the method by which it is measured does not account for the dependence of segregation on θ and the rheology that develops therein. Indeed, contact stress partitioning (detailed in Appendix C) relies heavily on the underlying assumption of how forces are split at large-small particle contacts. Future research dedicated to more objective stress partitioning is warranted.

The kinetic stress partition B^k on the other hand clearly changes with inclination and correlates better with the segregation rate trends in Figure 4c. Staron and Phillips (2014) have shown that in dry bi-disperse mixtures B^k linearly changes with the shear rate. The segregation timescale in turn decreases with shear rate, leading to the conclusion that greater B^k results in lower τ_s (Staron & Phillips, 2015). A similar correlation is observed in our results (Figure 9b). It is also consistent with previous results that the segregation rate correlates with the velocity difference between layers (Fan & Hill, 2011a, 2011b; Itoh & Hatano, 2019) and that large particles in chute flows are segregated towards the 'cooler' regions (near the free surface) of the flow (Dahl & Hrenya, 2004; Staron, & Phillips, 2014).

The lower B^k in the fluid saturated regimes indicates the effect of the ambient fluid in decreasing the shear rate and kinetic pressures. The decrease of B^k with inclination in the FI and VI regimes are possibly related to the formation of plug zones near the free surface (occupying about half of the total flow height) as shown in Figure 6. Physically, it can be reasoned that as the motion of large particles are partly driven by the shearing it experiences as it travels between flowing layers (Jing et al., 2017; Staron, 2018), the absence of a defined velocity gradient in the plug zone hinders their upward rise. In light of kinetic sieving, low $\dot{\gamma}$ also implies reduced generation of random voids (Drahun & Bridgwater, 1983), which, when coupled with the

reduced energetic motion, decreases the probability of small particles to fit into the available voids, leading to an overall reduction in the downward percolation velocity of small particles.

5.2 Implications for saturated mass flows

Size segregation, particularly inverse grading, is a common feature in geophysical flows though the extent to which it is observed varies from case to case. Field investigations and physical experiments show that inverse grading is less evident in highly saturated flows which suggests that solid-fluid interactions significantly affect particle dynamics (Major & Pierson, 1992; Zhou et al., 2019). This work only focuses on the case where the granular flows are dense and completely saturated. Granular flows are simulated according to the rheology that arises from solid-fluid interactions defined by the different flow regimes, instead of simply varying the fluid material properties; indeed, larger particles flowing in an ambient viscous fluid may behave like a fluid-inertial flow, while very fine particles flowing in water can fall into the viscous regime (Cassar et al., 2005; Jing et al., 2019). The findings imply that the degree of inverse grading observed in the deposits of geophysical mass flows can be used to evaluate the dominant transport mechanism during the course of its motion. This can be particularly useful in evaluating mass flow events which have completely dried up and whose previous state of saturation cannot be judged accurately. Evident inverse grading means that the flow is inertial, dominated by frictional-collisional interactions with minimal involvement from interstitial fluid. This can either mean that the interstitial fluid is not very viscous, is significantly less dense than the solid particles, or that the flowing particles are significantly large and massive. Consistently, inertial flows of dissimilarly sized granular mixtures result in efficient levee formation (Félix & Thomas, 2004; de Haas et al., 2015). On the other hand, poor inverse grading in the deposits would imply that the flow is viscous, which means that viscous dissipation is dominant and

segregation develops very slowly. Such flows usually involve very viscous slurries with high fines content and often correspond to poor levee formation (Zhou et al., 2019).

Segregation is considered to be a transient process and hence in geophysical flow models, which take size segregation into account, it is often assumed that size separation is fully-developed, i.e. small and large particles have completely separated. The presence of ambient fluids however results in longer segregation times, such that the mixture may still be well mixed during the entire duration of the flow. This may have implications in modelling levee formation (Baker et al., 2016) and breaking size segregation waves (van der Vaart et al., 2018) since such features require the large particles to be at the free surface for them to be easily and efficiently transported to the front or lateral sides of the flow. Lastly, the state of mixing and segregation in granular-fluid flows also have implications on its internal friction (Rognon et al., 2007; Yohannes & Hill, 2010; Tripathi & Khakhar, 2011).

6 Concluding remarks

Size segregation in saturated granular flows are studied using the numerical fluid-granular simulations. Granular flows are modelled according to three granular-fluid flow regimes – free-fall, fluid inertial, and viscous – where each regime exhibits distinct flow dynamics in which different rates of segregation are observed. It is found that, consistent with experiments, the presence of a viscous fluid effectively diminishes the degree of separation and slows down segregation.

Through detailed evaluation of different forcing terms in the momentum equation of the mixture theory of segregation, we find that the ambient fluid reduces segregation first by reducing the contact stress gradients through buoyant effects. The ambient fluid also slows down

segregation by reducing the shear rate, partly by inducing the formation of plug zones near the free surface where velocity gradients are greatly inhibited. This subtle dependence of segregation on rheology is reflected by kinetic stress partitioning, but not contact stress partitioning (likely because force splitting in the current partitioning method does not depend on flow information). The drag force in the normal direction does not directly hinder the upward rise of large particles regardless of the viscosity of the ambient fluid. The segregation velocity is therefore independent of viscosity and can be mainly written as a function of the flow shear rates and reduced pressures expressed in the form of a reduced inertial number.

The current work is an attempt to further understand the particle dynamics which develop under the influence of fluid interactions. A more detailed evaluation of the effects of viscosity and the relative density, in which the flow rheology is isolated, is warranted for better understanding the factors affecting segregation in solid-fluid mixture flows. It should also be noted that the system presented in this paper is somewhat different from actual granular-fluid chute flows in which the fluid phase flows along with (or independently from) the solid phase, though the segregation and rheology presented here are qualitatively consistent with such systems. Different fluid boundary conditions, such as periodic boundaries, may result in subtle differences in the segregation mechanisms. Nevertheless, the fluid effects determined in the study (i.e., buoyancy and reduced shear rates) are expected to be valid regardless of the boundary conditions and therefore are relevant to a wide range of fluid-granular flow scenarios.

A: The CFD-DEM method

The DEM and CFD modules are implemented using the open-source C++ libraries ESyS Particle (Weatherley et al., 2014) and OpenFOAM, respectively. The coupling between CFD and

DEM relies on a message passing algorithm that exchanges information between the DEM and the CFD through a dynamic linked library in which interaction forces are solved at fixed time intervals (Zhao, 2017).

In the DEM, the translational and rotational displacements of particles are calculated based on Newton's second law of motion and are updated after each numerical timestep. The governing equations can be written as:

$$m_j \frac{d^2 \boldsymbol{x_j}}{dt^2} = \sum_{\boldsymbol{c}} (\boldsymbol{f_{nc}} + \boldsymbol{f_{tc}}) + m_j \boldsymbol{g} + \boldsymbol{F_j^{F-G}} \tag{14}$$

$$\boldsymbol{I_j} \frac{d\boldsymbol{\omega_j}}{dt} = \sum_{c} \boldsymbol{r_c} \times \boldsymbol{f_{tc}} \tag{15}$$

Here, m_j and $\boldsymbol{x_j}$ are the mass and position of a particle *j* at a single numerical time-step, $\boldsymbol{I_j}$ is the moment of inertia of a sphere, $\boldsymbol{\omega_j}$ is the rotational acceleration, and $\boldsymbol{r_c}$ is the distance between the centers of two contacting spheres. $\boldsymbol{f_{nc}}$ and $\boldsymbol{f_{tc}}$ are the normal and tangential forces of particle-particle interactions defined at a contact point c, and are calculated according to the spring-dashpot model of Cundall & Strack, (1979):

$$\boldsymbol{f_{nc}} = K_n \delta_n \boldsymbol{n}_c + C_n \tag{16}$$

$$\boldsymbol{f_{tc}} = \min\{\boldsymbol{f_{tc}^{t-1}} + K_t \Delta \boldsymbol{v}_c^t, \mu \boldsymbol{f_{nc}}\} \tag{17}$$

where $K_n = \pi E(r_1 + r_2)/4$ and $K_t = \pi E(r_1 + r_2)/8(1 + G)$ are the particle normal and shear stiffness where E is Young's modulus, G is Poisson's ratio, and r_1 and r_2 are the radii of the contacting particles. δ_n is the overlapping distance between the two particles, $\Delta \boldsymbol{v}_c$ is the relative velocity of the contacting particles, and $\boldsymbol{n}_c$ is the unit vector of the contact normal. The damping force $C_n = 2\Omega\sqrt{K_n(m_1 + m_2)/2}$ is used to replicate the energy dissipation induced by plastic

deformation and shearing due to particle asperities. Ω is the damping coefficient, an empirical value related to the coefficient of restitution for collisional velocities. m_1 and m_2 are the masses of the contacting particles. $\boldsymbol{f_{tc}^{t-1}}$ and $\Delta \boldsymbol{v}_c^t$ are the tangential components of the force of the previous time step and relative contact velocities, respectively. μ is the contact friction coefficient.

The final term on the right hand side of equation (14) is the solid-fluid interaction force (Zhao, 2017):

$$\boldsymbol{F^{F-G}} = \boldsymbol{F_j^b} + \boldsymbol{F_j^d} = -V_j \nabla P_F + \frac{1}{2} C_d \rho_F \frac{\pi D^2}{4} |\boldsymbol{U_F} - \boldsymbol{U_G}| (\boldsymbol{U_F} - \boldsymbol{U_G}) \Phi_F^{(1-\chi)} \tag{18}$$

As presented in 2.1, $\boldsymbol{F_j^b}$ is the buoyant force where V_j is the volume of a particle j and ∇P_F is the fluid pressure gradient. $\boldsymbol{F_j^d}$ is the drag force which quantifies the force acting opposite to the relative velocity between the particle and the surrounding fluid. The drag force equation proposed by Di Felice (1994) is used in this study where:

$$C_d = \frac{24}{Re}(1 + 0.15Re^{0.681}) + \frac{0.407}{1 + \frac{8710}{Re}} \tag{19}$$

$$Re = \rho_F d |\boldsymbol{U_F} - \boldsymbol{U_G}| / \eta_F \tag{20}$$

are the drag coefficient and Reynold's number defined at the particle scale, respectively. $\boldsymbol{U_F}$ and $\boldsymbol{U_G}$ are the fluid and particle velocities, ρ_F is the fluid density, and η_F is the dynamic viscosity. The term $\Phi_F^{(1-\chi)}$ is an empirical relationship introduced to express the influence of particle concentration on the drag coefficient where $\chi = 3.7 - 0.65\exp\left[-\frac{(1.5-\log_{10} Re)^2}{2}\right]$. The form of the drag law presented in equation (19) is chosen for its ability to correctly model the drag coefficient for a wide range of Re (Zhao, 2017).

739 The fluid domain is discretized into three-dimensional cells where the Navier-Stokes
740 equations are solved using the Finite Volume Method (FVM) (Anderson, 1995). The mass and
741 momentum continuum equations are written as:

$$\frac{\partial(\Phi_F \rho_F)}{\partial t} + \nabla \cdot (\Phi_F \rho_F \boldsymbol{U_F}) = 0 \tag{21}$$

$$\frac{\partial(\Phi_F \rho_F \boldsymbol{U_F})}{\partial t} + \nabla \cdot (\Phi_F \rho_F \boldsymbol{U_F} \otimes \boldsymbol{U_F}) - \Phi_F \nabla \cdot S_F = -\Phi_F \nabla P_F + \Phi_F \rho_F \boldsymbol{g} + \boldsymbol{f_d} \tag{22}$$

742 where S_F is the fluid stress tensor calculated via the standard $k - \varepsilon$ turbulence model (Zhao,
743 2017). The term $\boldsymbol{f_d} = \sum_{j=1}^{N} {F_j^d}/{V_{fc}}$ is the drag force per unit fluid volume where V_{fc} is the fluid
744 cell volume. The fluid pressures and velocities that are calculated in each cell are used, in turn, to
745 calculate the interaction forces.

746 **B: Averaging method**

747 To calculate the relevant kinematic and rheological properties, the entire flow is divided
748 into sampling volumes with fixed dimensions $V_M = 35d_S \times 10d_S \times \Delta z$, where $\Delta z = d_L$. These
749 properties are calculated considering the contribution of the part of each particle that falls within
750 Δz centered at a height z. For a granular flow with total flow velocity $\boldsymbol{U_G} = u\hat{\boldsymbol{x}} + v\hat{\boldsymbol{y}} + w\hat{\boldsymbol{z}}$, the
751 volume fractions Φ_i and streamwise velocities u_i for particles of species i are calculated as (Fan
752 et al., 2014a; Hill & Tan, 2014):

$$\Phi_i(z) = \frac{\sum_j V_{ij}}{V_M} \tag{23}$$

$$u_i(z) = \frac{\sum_j u_{ij} V_{ij}}{\sum_j V_{ij}} \tag{24}$$

753 respectively. V_{ij} and u_{ij} are the fractional volumes and velocities of a particle j of size species i.
754 Species local volume concentrations are calculated as $\phi_i = \Phi_i / \sum_{L,S} \Phi_i$. The shear rate is
755 calculated as the derivative of the time-averaged velocities $\dot{\gamma} = \left| {du}/{dz} \right|$. The segregation
756 velocity is calculated as $w_{p,i} = w_i - w$, where w is the local normal average velocity at z, and
757 w_i is the local averaged velocity of a particle.

758 The partial kinetic stress tensor is calculated as:

$$\boldsymbol{\sigma}_i^k(z) = \frac{1}{V_M} \sum_j m_{ij} \boldsymbol{\Lambda}_{ij} \otimes \boldsymbol{\Lambda}_{ij} \tag{25}$$

759 where $\boldsymbol{\Lambda}_{ij}$ is the fluctuating velocity of a particle j of species i, defined as the difference of the
760 instantaneous and time-averaged velocities, where the latter is calculated as $w(z) =$
761 $\sum_i \big(\Phi_i(z) w_i(z)\big) / \sum_i \Phi_i(z)$. The contact stress tensor is calculated as:

$$\boldsymbol{\sigma}_i^c(z) = \frac{1}{V_M} \left[\sum_{j \neq m} \boldsymbol{F}_{i,jm} \otimes \boldsymbol{l}_{i,jm} \right] \tag{26}$$

762 where $\boldsymbol{F}_{i,jm} = \boldsymbol{f_{nc}} + \boldsymbol{f_{tc}}$ is the contact force between particles j and m, where j is a particle
763 belonging to size species i, and $\boldsymbol{l}_{i,jm}$ is the distance between their centers,. Assuming that the
764 normal stress is isotropic in all directions, contact and kinetic partial pressures are calculated as
765 $P_i^c = \boldsymbol{\sigma}_i^{c,zz}$ and $P_i^k = \boldsymbol{\sigma}_i^{k,zz}$, respectively. Total partial pressure is $P_i = P_i^c + P_i^k$ and bulk
766 pressure is calculated as $P = P_L + P_S$. Contact and kinetic pressure fractions are calculated
767 as $\psi_i^c = P_i^c / P^c$ and $\psi_i^k = P_i^k / P^k$, respectively.

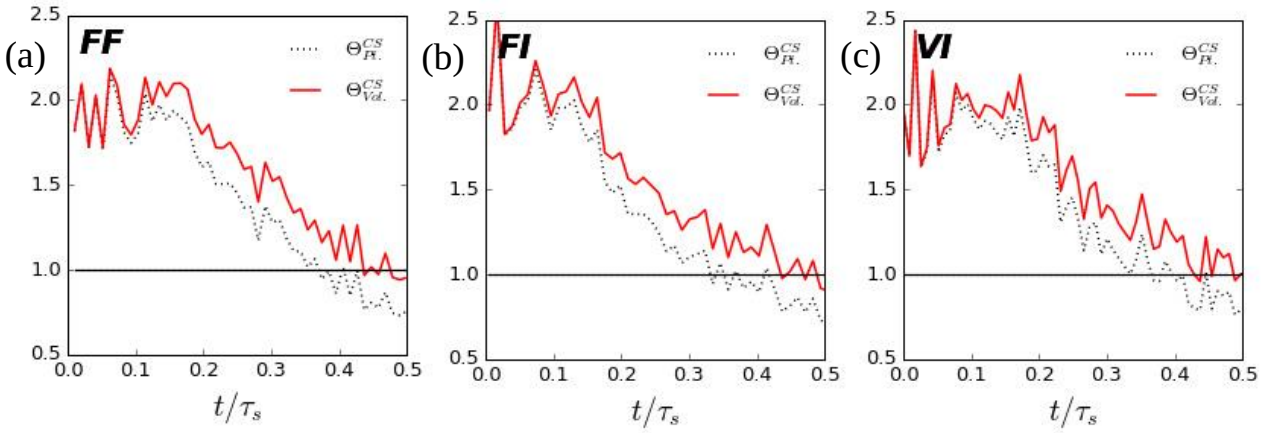

Figure 14. The effect of radius- and volume-based partitioning on the depth-averaged contact stress gradients in the (a) FF, (FI), and (c) VI regimes.

Data is recorded at every computational time step of 0.1 seconds (10 Hz). Calculation of relevant parameters are taken at specific time intervals over 20 such time steps. Values calculated using equations (23)-(26) are smoothened over 10 time intervals centered at a chosen time step.

C: Contact stress partitioning

The calculation of the contact pressure, the pressure fraction, and partition coefficient are greatly affected by how the contact forces are partitioned among differently sized constituents. The conclusions one can make based on the contact stresses can vary depending on the choice of partitioning function. Here, we briefly discuss the effects of choosing partition forces based on the relative radius or volume of contacting particles. Contact stresses, for differently sized particles, partitioned based on the radius ratio (i.e., at the point of contact) are calculated as:

$$\boldsymbol{\sigma}_i^c = \boldsymbol{F}_{i,LS} \otimes \left(\frac{r_i}{r_L + r_S}\right) \boldsymbol{l}_{LS} \tag{27}$$

where r_i is the radius of the particle specie i. Contact stresses partitioned according to the volume of contacting particles are calculated as:

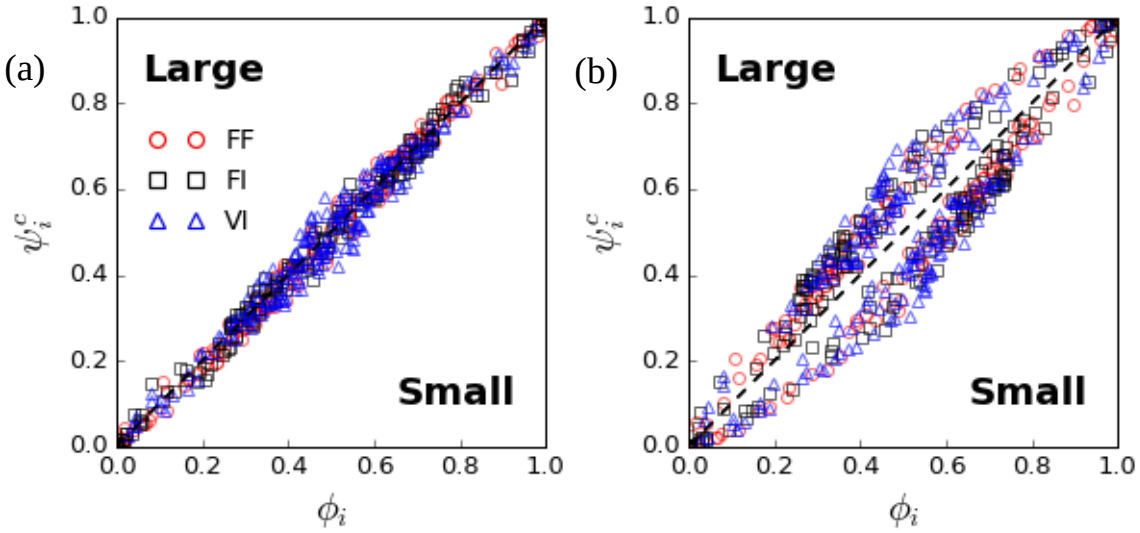

Figure 15. The contact pressure fraction ψ_i^c as a function of the local concentration ϕ_i for mixtures in different regimes flowing at 22° for forces partitioned according to the (a) radii and (b) volumes of contacting particles.

$$\boldsymbol{\sigma}_i^c = \boldsymbol{F}_{i,LS} \otimes \left(\frac{r_i^3}{r_L^3 + r_S^3} \right) \boldsymbol{l}_{LS} \tag{28}$$

As shown in Figure 14, the contact stresses calculated using the radius-based partitioning are smaller than that the volume-based partitioning, regardless of the flow regime. The two trends separate as the mixture segregates and the interaction between large and small particles are maximum. Figure 15 shows that using the contact-point partitioning the contact stress fraction appears to be equal to the local concentration, such that B^c is very small, implying that contact stresses do not drive segregation at all and simply work to balance the large particles' weight (similar to Hill & Tan 2014). On the other hand, partitioning according to the volume of contacting particles would result in an asymmetry in the contact stresses where the large particles receive a larger portion which then leads one to infer that contact stresses do in fact drive segregation. The latter method is considered to be more reasonable, and used in the main text, as recent segregation force studies showed clearly that rising of large particles is a result of net contact forces overcoming the particle weight (Guillard et al., 2016; van der Vaart et al., 2018).

Besides, a volume-based partitioning funciton in Tunuguntla et al. (2014) was reported to produce good prediction of size- and density-segregation.

D: Calculation of c_{PI} and c_D

Solving the momentum equation in the mixture theory requires determination of the linear drag coefficient c_{PI} and diffusion coefficient c_D. According to Gray and Chugunov (2006), the diffusion coefficient can be expressed as $c_D = c_{PI}D$, where D is the diffusivity which measures the ability of a particle to randomly disperse throughout the mixture due to random collisions. D can be determined independently from the other components of the momentum equation through the mean squared displacements (MSD) of individual particles $\langle \Delta z(\Delta t)^2 \rangle = 2D\Delta t$, where $\Delta z(\Delta t) = z(t_0 + \Delta t) - z(t_0) - \int_{t_0}^{t_0+\Delta t} w(t)dt$ is the non-affine part of the particle trajectory along the normal direction per unit time, and $\langle x \rangle$ represents ensemble averaging within a flowing layer (Fan et al., 2014). Using the calculated values, c_D can then be obtained by finding the corresponding value that will provide the best-fit for the following balance equation (which assumes steady state):

$$c_{PI} = \frac{\frac{\partial P_i}{\partial z} - \Phi_i \rho_i g}{-\left[\Phi_i \rho_i (w_i - w) + \rho_G D \frac{\partial \phi_i}{\partial z}\right]} \tag{29}$$

The determined c_{PI} value is then multiplied by D to calculate the diffusion coefficient c_D.

E: Formation of plug zones

As particles move within an ambient fluid they experience a drag force F^d which counteracts the flow. Although there are two fluid forces considered here, it is only F^d which works opposite to the flow direction. Figures 16a and 16b show the drag force F^d along the

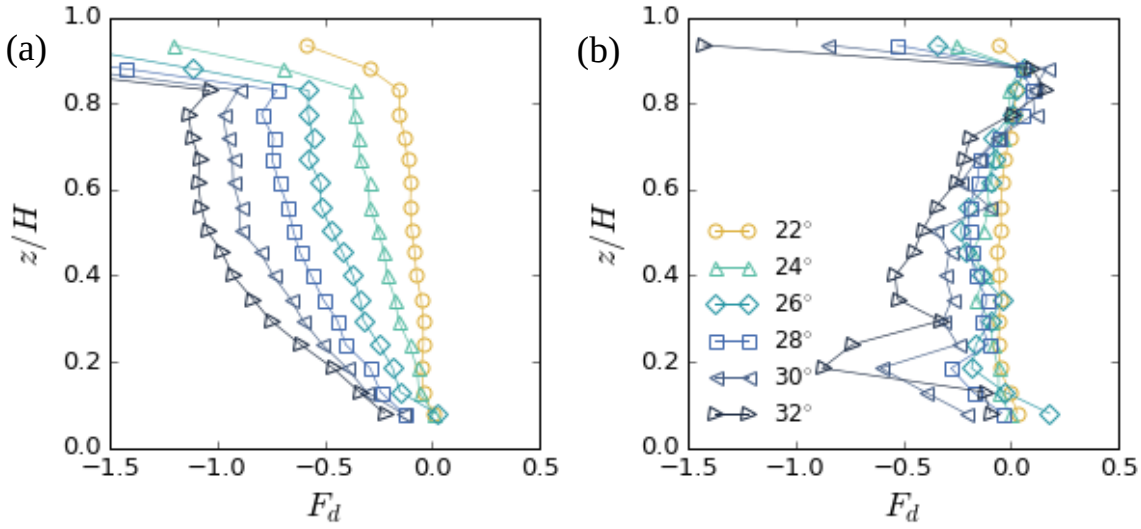

Figure 16. Dimensionless drag force F_d in the flow direction in the (a) FI and (b) VI regimes.

stream-wise direction in the FI and VI regimes, respectively, normalized by the buoyant weight (averaged over $t = 0.1{\sim}0.5\tau_s$). As calculated from equation (18), F^d is negative when the solid phase flows faster than the fluid phase. F^d in FI becomes increasingly negative with θ and is highest near the free surface. This increasing resistive force leads to the formation of plug zones in the u profiles of FI. The abrupt increase at the topmost part is due to the low fluid flow velocity at the boundary of the fluid and mixture free surface. The F^d in the VI are surprisingly lower than in FI despite being more viscous mainly because the relative velocities between the solid and fluid phases are low. For $\theta = 22°{\sim}26°$, F^d in VI does not significantly increase (negatively) and only appears to fluctuate around 0. F^d slightly increases at the higher angles $\theta = 28°{\sim}32°$, manifested through large fluctuations within the flow body.

F: Segregation velocities in different flow regimes

Figure 17 shows raw segregation velocities $w_{p,i}$ for varying slope angels in each flow regime. Data in each regime practically follow the same trend and can therefore be taken as a single data set. There are subtle differences in the fitted slopes between samples at different θ but

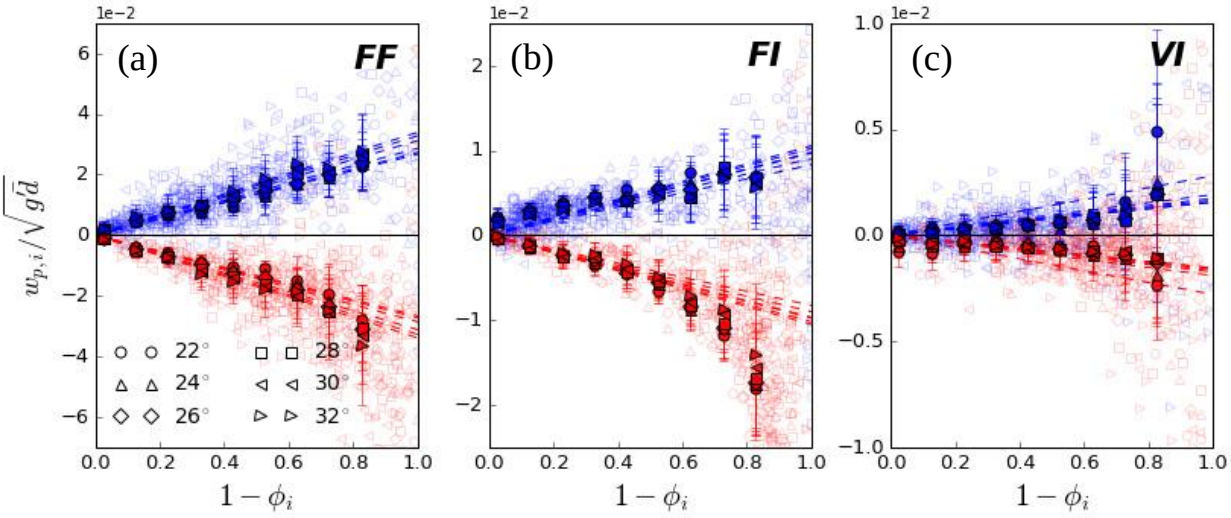

Figure 17. The normalized segregation velocities $w_{p,i}$ for every θ in (a) FF, (b) FI, and (c) VI. The solid markers indicate the mean $w_{p,i}$ and the background markers are the raw data. Blue markers represent $w_{p,i}$ for large particles and red markers are for the small particles. The dashed lines are the slopes of the mean $w_{p,i}$; the small and large particles have equal slopes but different signs.

are much lower than the differences between flow regimes. The solid symbols are the mean $w_{p,i}$ averaged over $1-\phi_i = 0.1$ while the lightly shaded symbols are all the $w_{p,i}$ for all values of θ.

Acknowledgments

The authors acknowledge financial support from the National Natural Science Foundation of China (grant nos. 41941017, 11672318), Key Research Program of Frontier Sciences, Chinese Academy of Sciences (CAS) (grant no. QYZDB-SSW-DQC010), and the CAS-TWAS President's Fellowship for International PhD students. Data and codes that can be used to replicate and validate the results presented here are available through the following link: http://doi.org/10.5281/zenodo.3663215.

References

Amarsid, L., Delenne, J. Y., Mutabaruka, P., Monerie, Y., Perales, F., & Radjai, F. (2017).

Viscoinertial regime of immersed granular flows. *Physical Review E*, *96*(1). doi:10.1103/PhysRevE.96.012901

Anderson, J.D. (1995). Coputational fluid dynamics: The basics with applications. McGraw-Hill

Bagnold, R. A. (1954). Experiments on a Gravity-free Dispersion of Large Solid Spheres in a Newtonian Fluid under Shear. *Proceedings of the Royal Society A*, *225*(1160), 49–63.

Baker, J., Gray, J. M. N. T., & Kokelaar, B. P. (2016). Particle Size-Segregation and Spontaneous Levee Formation in Geophysical Granular Flows. *International Journal of Erosion*, *9*(4), 174–178.

Baker, J. L., Johnson, C. G., & Gray, J. M. N. T. (2016). Segregation-induced finger formation in granular free-surface flows. *Journal of Fluid Mechanics*, *809*, 168–212. doi:10.1017/jfm.2016.673

Cassar, C., Nicolas, M., & Pouliquen, O. (2005). Submarine granular flows down inclined planes. *Physics of Fluids*, *17*(10). doi:10.1063/1.2069864

Courrech du Pont, S., Gondret, P., Perrin, B., & Rabaud, M. (2003). Granular Avalanches in Fluids. *Physical Review Letters*, *90*(4), doi:10.1103/PhysRevLett.90.044301

Coussot, P., & Meunier, M. (1996). Recognition, classification and mechanical description of debris flows. *Earth-Science Reviews*, *40*(3–4), 209–227, doi:10.1016/0012-8252(95)00065-8

Cundall, P. A., & Strack, O. D. L. (1979). A discrete numerical model for granular assemblies. *Géotechnique*, *29*(1), 47–65, doi: 10.1680/geot.1979.29.1.47

Dahl, S. R., & Hrenya, C. M. (2004). Size segregation in rapid, granular flows with continuous size distributions. *Physics of Fluids*, *16*(1), 1–13. doi:10.1063/1.1626682

De Haas, T., Braat, L., Leuven, J. R. F. W., Lokhorst, I. R., & Kleinhans, M. G. (2015). Effects of debris flow composition on runout, depositional mechanisms, and deposit morphology in laboratory experiments. *Journal of Geophysical Research F: Earth Surface*, *120*(9), 1949–1972. doi:10.1002/2015JF003525

Drahun, J. A., & Bridgwater, J. (1983). The mechanisms of free surface segregation. *Powder Technology*, *36*(1), 39–53. doi:10.1016/0032-5910(83)80007-2

Fan, Y., & Hill, K. M. (2011a). Phase transitions in shear-induced segregation of granular materials. *Physical Review Letters*, *106*(21), doi:10.1103/PhysRevLett.106.218301

Fan, Y., & Hill, K. M. (2011b). Theory for shear-induced segregation of dense granular mixtures. *New Journal of Physics*, *13*. doi:10.1088/1367-2630/13/9/095009

Fan, Y., Schlick, C. P., Umbanhowar, P. B., Ottino, J. M., & Lueptow, R. M. (2014). Modelling size segregation of granular materials: The roles of segregation, advection and diffusion.

Journal of Fluid Mechanics, *741*, 252–279. doi:10.1017/jfm.2013.680

Félix, G., & Thomas, N. (2004). Relation between dry granular flow regimes and morphology of deposits: Formation of levées in pyroclastic deposits. *Earth and Planetary Science Letters*, *221*(1–4), 197–213. doi:10.1016/S0012-821X(04)00111-6

Ferdowsi, B., Ortiz, C. P., Houssais, M., & Jerolmack, D. J. (2017). River bed armoring as a granular segregation phenomenon. *Nature Communications*, *8*(1363), 10. doi:10.1038/s41467-017-01681-3

Fry, A. M., Umbanhowar, P. B., Ottino, J. M., & Lueptow, R. M. (2018). Effect of pressure on segregation in granular shear flows. *Physical Review E*, *97*(6), 062906. https://doi.org/10.1103/PhysRevE.97.062906

Gajjar, P., & Gray, J. M. N. T. (2014). Asymmetric flux models for particle-size segregation in granular avalanches. *Journal of Fluid Mechanics*, *757*, 297–329. doi:10.1017/jfm.2014.503

Gray, J. M.N.T., & Chugunov, V. A. (2006). Particle-size segregation and diffusive remixing in shallow granular avalanches. *Journal of Fluid Mechanics*, 569, doi:10.1017/S0022112006002977

Gray, J. M.N.T., & Ancey, C. (2009). Segregation, recirculation and deposition of coarse particles near two-dimensional avalanche fronts. *Journal of Fluid Mechanics*, *629*, 387–423. doi:10.1017/S0022112009006466

Gray, J.M.N.T. (2018). Particle Segregation in Dense Granular Flows. *Annu. Rev. Fluid Mech*, *50*, 407–433. doi:10.1146/annurev-fluid-122316

Gray, J.M.N.T, & Thornton, A.R. (2005). A theory for particle size segregation in shallow granular free-surface flows. *Proceedings of the Royal Society A*, *461*, 1447–1473. doi:10.1098/rspa.2004.1420

Guillard, F., Forterre, Y., & Pouliquen, O. (2016a). Scaling laws for segregation forces in dense sheared granular flows. *Journal of Fluid Mechanics*, *807*, doi:10.1017/jfm.2016.605

Hill, K. M., & Tan, D. S. (2014). Segregation in dense sheared flows: Gravity, temperature gradients, and stress partitioning. *Journal of Fluid Mechanics*, *756*, 54–88. doi:10.1017/jfm.2014.271

Ilstad, T., Elverhoi, A., Issler, D., & Marr, J.G. (2004). Subaqueous debris flow behaviour and its dependence on the sand/clay ratio : a laboratory study using particle tracking. *Marine Geology*, *213*, 415–438. doi:10.1016/j.margeo.2004.10.017

Itoh, R., & Hatano, T. (2019). Geological implication of grain-size segregation in dense granular matter. *Philosophical Transactions of the Royal Society A: Mathematical, Physical and Engineering Sciences*, *377*(2136). doi:10.1098/rsta.2017.0390

Iverson, R. M. (1997). The Physics of Debris Flows. *Reviews of Geophysics*, *35*(3), 245–296,

906 doi:10.1029/97RG00426

907 Jing, L., Kwok, C. Y., & Leung, Y. F. (2017). Micromechanical Origin of Particle Size
908 Segregation. *Physical Review Letters*, *118*(11).
909 https://doi.org/10.1103/PhysRevLett.118.118001

910 Jing, L., Yang, G. C., Kwok, C. Y., & Sobral, Y. D. (2019). Flow regimes and dynamic
911 similarity of immersed granular collapse : A CFD-DEM investigation. *Powder Technology*,
912 *345*, 532–543. https://doi.org/10.1016/j.powtec.2019.01.029

913 Johnson, C. G., Kokelaar, B. P., Iverson, R. M., Logan, M., Lahusen, R. G., & Gray, J. M. N. T.
914 (2012). Grain-size segregation and levee formation in geophysical mass flows. *Journal of*
915 *Geophysical Research*, (March). https://doi.org/10.1029/2011JF002185

916 Jones, R.P., Isner, A.B., Xiao, H.Y., Ottino, J.M., Umbanhowar, P.B., & Lueptow, R.M. (2018).
917 Asymmetric dependence of segregation fluxes in granular flows. *Physical Review Fluids*,
918 3(9), http://doi.org/10.1103/PhysRevFluids.3.094304.

919 Kleinhans, M. G. (2004). Sorting in grain flows at the lee side of dunes. *Earth-Science Reviews*,
920 *65*, 75–102. https://doi.org/10.1016/S0012-8252(03)00081-3

921 Kokelaar, B. P., Graham, R. L., Gray, J. M. N. T., & Vallance, J. W. (2014). Fine-grained linings
922 of leveed channels facilitate runout of granular flows. *Earth and Planetary Science Letters*,
923 *385*, 172–180. https://doi.org/10.1016/j.epsl.2013.10.043

924 Lai, Z., Vallejo, L. E., Zhou, W., Ma, G., Espitia, J. M., Caicedo, B., & Chang, X. (2017).
925 Collapse of granular columns with fractal particle size distribution: implications for
926 understanding the role of small particles in granular flows. *Geophysical Research Letters*,
927 *44*(24), 12,181-12,189. https://doi.org/10.1002/2017GL075689

928 Linares-Guerrero, E., Goujon, C., & Zenit, R. (2007). Increased mobility of bidisperse granular
929 avalanches. *Journal of Fluid Mechanics*, *593*, 475–504.
930 https://doi.org/10.1017/S0022112007008932

931 Mainali, A., & Rajaratnam, N. (1994). Experimental Study of Debris Flows. *Journal of*
932 *Hydraulic Engineering*, *120*(1), 104–123.

933 Major, J. J., & Pierson, T. C. (1992). Debris flow rheology: Experimental analysis of fine-
934 grained slurries. *Water Resources Research*, *28*(3), 841–857, doi:10.1029/91WR02834

935 Mandal, S., & Khakhar, D. V. (2019). Dense granular flow of mixtures of spheres and dumbbells
936 down a rough inclined plane: Segregation and rheology. *Physics of Fluids*, *31*(2),
937 doi:10.1063/1.5082355

938 May, L. B. H., Golick, L. A., Phillips, K. C., Shearer, M., & Daniels, K. E. (2010). Shear-driven
939 size segregation of granular materials: Modeling and experiment. *Physical Review E*, *81*(5),
940 2–9, doi:10.1103/PhysRevE.81.051301

Midi, G. D. R. (2004). On dense granular flows. *European Physical Journal E*, *14*(4), 341–365. doi:10.1140/epje/i2003-10153-0

Mulder, T., & Alexander, J. (2001a). The physical character of subaqueous sedimentary density flow and their deposits. *Sedimentology*, *48*(2), 269–299. doi:10.1046/j.1365-3091.2001.00360.x

Rognon, P. G., Roux, J. N., Naaïm, M., & Chevoir, F. (2007). Dense flows of bidisperse assemblies of disks down an inclined plane. *Physics of Fluids*, *19*(5), 7–11. doi:10.1063/1.2722242

Savage, S. B., & Hutter, K. (1989). The motion of a finite mass of granular material down a rough incline. *Journal of Fluid Mechanics*, *199*(2697), 177–215, doi:10.1017/S0022112089000340

Savage, S. B., & Lun, C. K. K. (1988). Particle size segregation in inclined chute flow of dry cohesionless granular solids. *Journal of Fluid Mechanics*, *189*, 311–335, doi:10.1017/S002211208800103X

Schlick, C. P., Fan, Y., Isner, A. B., Umbanhowar, P. B., Ottino, J. M., & Lueptow, R. M. (2015). Modeling Segregation of bidisperse granular materials using physical control parameters in the quasi-2D bounded heap. *Journal of the American Institute of Chemical Engineers*, *61*(5). doi:10.1002/aic.14780

Siman-Tov, S., & Brodsky, E. E. (2018). Gravity-Independent Grain Size Segregation in Experimental Granular Shear Flows as a Mechanism of Layer Formation. *Geophysical Research Letters*, *45*(16), 8136–8144, doi:10.1029/2018GL078486

Staron, L., & Phillips, J. C. (2014). Segregation time-scale in bi-disperse granular flows. *Physics of Fluids*, *26*(3), doi:10.1063/1.4867253

Staron, L., & Phillips, J. C. (2015). Stress partition and microstructure in size-segregating granular flows, *022210*, 1–8, doi:10.1103/PhysRevE.92.022210

Staron, L. (2018). Rising dynamics and lift effect in dense segregating granular flows. *Physics of Fluids*, *30*(12). doi:10.1063/1.5045576

Thornton, A. R., Gray, J. M. N. T., & Hogg, A. J. (2006). A three-phase mixture theory for particle size segregation in shallow granular free-surface flows. *Journal of Fluid Mechanics*, *550*, 1–25, doi:10.1017/S0022112005007676

Tripathi, A., & Khakhar, D. V. (2011). Rheology of binary granular mixtures in the dense flow regime. *Physics of Fluids*, *23*(11), doi:10.1063/1.3653276

Tripathi, A., & Khakhar, D. V. (2013). Density difference-driven segregation in a dense granular flow. *Journal of Fluid Mechanics*, *717*, 643–669, doi:10.1017/jfm.2012.603

Trulsson, M., Andreotti, B., & Claudin, P. (2012). Transition from the viscous to inertial regime

in dense suspensions. *Physical Review Letters*, *109*(11), 1–5, doi:10.1103/PhysRevLett.109.118305

Tunuguntla, D. R., Bokhove, O., & Thornton, A. R. (2014). A mixture theory for size and density segregation in shallow granular free-surface flows. *Journal of Fluid Mechanics*, *749*(2014), 99–112, doi:10.1017/jfm.2014.223

Tunuguntla, Deepak R., Weinhart, T., & Thornton, A. R. (2016). Comparing and contrasting size-based particle segregation models. *Computational Particle Mechanics*, doi:10.1007/s40571-016-0136-1

Umbanhowar, P. B., Lueptow, R. M., & Ottino, J. M. (2019). Modeling Segregation in Granular Flows. *Annual Review of Chemical and Biomolecular Engineering*, *10*, 1–25, doi:10.1146/annurev-chembioeng-060718-030122

van der Vaart, K., Lantman, M. P. V. S., Weinhart, T., Luding, S., Ancey, C., & Thornton, A. R. (2018). Segregation of large particles in dense granular flows suggests a granular Saffman effect. *Physical Review Fluids*, *074303*, 1–12. doi:10.1103/PhysRevFluids.3.074303

van der Vaart, K., Gajjar, P., Epely-Chauvin, G., Andreini, N., Gray, J. M. N. T., & Ancey, C. (2015). Underlying Asymmetry within Particle Size Segregation. *Physical Review Letters*, *114*(23), 1–5. https://doi.org/10.1103/PhysRevLett.114.238001

van der Vaart, K., Thornton, A. R., Johnson, C. G., Weinhart, T., Jing, L., Gajjar, P., … Ancey, C. (2018). Breaking size-segregation waves and mobility feedback in dense granular avalanches. *Granular Matter*, *20*(3). doi:10.1007/s10035-018-0818-x

Weatherley, D., Hancock, W., Boros, V., & Abe, S. (2014). ESyS-Particle Tutorial and User's Guide Version 2.3.1, 1–152.

Weinhart, T, Luding, S., & Thornton, A. R. (2013). From Discrete Particles to Continuum Fields in Mixtures, *1202*, doi:10.1063/1.4812153

Weinhart, T., & Thornton, A. R. (2017). Comparing and contrasting size-based particle segregation models: applying coarse-graining to perfectly bidisperse systems. *Computational Particle Mechanics*, *4*(4), 387–405, doi:10.1007/s40571-016-0136-1

Yohannes, B., & Hill, K. M. (2010). Rheology of dense granular mixtures: Particle-size distributions, boundary conditions, and collisional time scales. *Physical Review E*, 82(6), 1–9, doi:10.1103/PhysRevE.82.061301

Zanuttigh, B., & Ghilardi, P. (2010). Segregation process of water-granular mixtures released down a steep chute. *Journal of Hydrology*, *391*(1–2), 175–187, doi:10.1016/j.jhydrol.2010.07.016

Zhao, T., Houlsby, G. T., & Utili, S. (2014). Investigation of granular batch sedimentation via DEM–CFD coupling. *Granular Matter*, *16*(6), 921–932. doi:10.1007/s10035-014-0534-0

Zhao, Tao. (2017). Coupled DEM-CFD analyses of landslide-induced debris flows.

Zhao, Y., Xiao, H., Umbanhowar, P. B., & Lueptow, R. M. (2018). Simulation and modeling of segregating rods in quasi-2D bounded heap flow, *64*(5). https://doi.org/10.1002/aic.16035

Zhou, G. G. D., Li, S., Song, D., Choi, C. E., & Chen, X. (2019). Depositional mechanisms and morphology of debris flow: physical modelling. *Landslides*, *16*(2), 315–332, doi:10.1007/s10346-018-1095-9

Zhou, G. G. D., & Ng, C. W. W. (2010). Numerical investigation of reverse segregation in debris flows by DEM. *Granular Matter*, *12*(5), 507–516, doi:10.1007/s10035-010-0209-4

Zhou, G. G. D., & Sun, Q. C. (2017). Study of Pore Fluid Effect on the Mobility of Granular Debris Flows. In *Powders and Grains*, 09046, 1–4.